nature immunology

Article

https://doi.org/10.1038/s41590-023-01475-4

TREM2 macrophages drive NK cell paucity and dysfunction in lung cancer

Received: 30 June 2022

Accepted: 23 February 2023

Published online: 20 April 2023

Check for updates

Matthew D. Park[1,2,3,13], Ivan Reyes-Torres[1,2,3,13], Jessica LeBerichel[1,2,3], Pauline Hamon[1,2,3], Nelson M. LaMarche[1,2,3,4], Samarth Hegde[1,2,3], Meriem Belabed[1,2,3], Leanna Troncoso[1,2,3], John A. Grout[1,2,3], Assaf Magen[1,2,3], Etienne Humblin[1,2,3], Achuth Nair[1,2,3], Martina Molgora[5], Jinchao Hou[5], Jenna H. Newman[1,2,6], Adam M. Farkas[1,2,6], Andrew M. Leader[1,2,3,9], Travis Dawson[1,2,3,7], Darwin D'Souza[1,2,3,7], Steven Hamel[1,2,3], Alfonso Rodriguez Sanchez-Paulete[1,2,3], Barbara Maier[1,2,3,10], Nina Bhardwaj[1,2,3,6], Jerome C. Martin[1,2,3,11], Alice O. Kamphorst[1,2,3], Ephraim Kenigsberg[1,8], Maria Casanova-Acebes[1,2,3,12], Amir Horowitz[1,2,3], Brian D. Brown[1,2,3,8], Lucas Ferrari De Andrade[1,2,3], Marco Colonna[5], Thomas U. Marron[1,2,3,4,6] & Miriam Merad[1,2,3,4,7,8]

Natural killer (NK) cells are commonly reduced in human tumors, enabling many to evade surveillance. Here, we sought to identify cues that alter NK cell activity in tumors. We found that, in human lung cancer, the presence of NK cells inversely correlated with that of monocyte-derived macrophages (mo-macs). In a murine model of lung adenocarcinoma, we show that engulfment of tumor debris by mo-macs triggers a pro-tumorigenic program governed by triggering receptor expressed on myeloid cells 2 (TREM2). Genetic deletion of *Trem2* rescued NK cell accumulation and enabled an NK cell-mediated regression of lung tumors. TREM2$^+$ mo-macs reduced NK cell activity by modulating interleukin (IL)-18/IL-18BP decoy interactions and IL-15 production. Notably, TREM2 blockade synergized with an NK cell-activating agent to further inhibit tumor growth. Altogether, our findings identify a new axis, in which TREM2$^+$ mo-macs suppress NK cell accumulation and cytolytic activity. Dual targeting of macrophages and NK cells represents a new strategy to boost antitumor immunity.

Antitumor immunity is constrained by several variables, including the dysfunction of chronically stimulated, exhausted T cells and the unique ability for tumor cells to escape recognition and killing by T cells[1]. While various modalities of immunotherapy focus on dysfunctional T cells, designing tools that empower NK cells, which are not dependent on tumor antigen-specific recognition, represents an attractive alternative[2]. But, while NK cells have been linked to better control of tumor growth and metastases, they are scarce in both human and murine tumor lesions[3,4]. The reasons why they are so often excluded from the tumor bed and why the NK cells that do infiltrate exhibit a highly dysfunctional phenotype with low cytolytic potential remain unclear. Indeed, some tumors actively evade NK cell-mediated killing by either downregulating or shedding activating surface ligands (for example, NKG2D ligands) or upregulating inhibitory ones[5,6]. Notably, known inhibitory receptors that mediate and maintain NK cell de-activation also recognize major histocompatibility (MHC) class I machinery, including HLA-A, HLA-B, HLA-C and HLA-E[7], which are already often suppressed by tumors so as to escape pressure from tumor-infiltrating CD8$^+$ T cells[8,9]; however, while tumors with low MHC-I may resist CD8$^+$ T cell activity, they should be vulnerable to NK cell cytotoxicity, so

A full list of affiliations appears at the end of the paper. e-mail: miriam.merad@mssm.edu

identifying the mechanisms that impair NK cells and strengthening NK cells in tumors would reinforce immunosurveillance and control elusive tumors[10,11]. Which cellular players of the tumor microenvironment (TME) contribute to the paucity and dysfunction of NK cells has yet to be fully elucidated.

Our groups and others have found that many human tumor lesions are deprived of NK cells and are heavily infiltrated by mo-macs[12–14]. Mo-macs are purportedly immunosuppressive[15,16], but targeting them has proven difficult, in part due to a limited understanding of the heterogeneity of macrophage states that are present in the TME[17], thus highlighting the need to dissect and characterize the role of these programs in the generation and maintenance of an antitumor response[18]. For instance, we demonstrated that, in tumor inception, tissue-resident macs (RTMs) physically interact with early tumor cells, promoting epithelial–mesenchymal transition and recruiting regulatory T (T_{reg}) cells to the early tumor niche[19], before being excluded to the periphery of the tumor[19,20]. Defining the molecular signature of mo-macs that supplant RTMs during later stages of tumor growth and characterizing their functional roles and how to modulate their immunosuppressive functions may augment the effect of cancer immunotherapy.

We demonstrated that, in both human and murine lung tumors, mo-macs express TREM2 (refs. 12,13,19). Though originally described in microglia as a phagocytic receptor for myelin debris[21–24], analogous populations of TREM2$^+$ mo-macs have been identified in multiple human and murine tumors. In models of sarcoma and ovarian cancer, TREM2 blockade generated an enhanced CD8$^+$ T cell response that delayed tumor growth and synergized with immune-checkpoint blockade[25–27], suggesting an immunosuppressive role for TREM2 in antitumor immunity; however, the most recent work on hepatocellular carcinoma showed that TREM2$^+$ macrophages may, in fact, limit tumor progression in the hepatic TME, suggesting that the functional contribution of these phagocytes to antitumor immunity is tissue-specific[28–30].

Therefore, in this study, we investigated the role that TREM2$^+$ mo-macs play in the development of non-small cell lung cancer (NSCLC), using the *Kras*$^{G12D/+}$*p53*$^{-/-}$ (KP) model of primary lung adenocarcinoma[31]. We found that phagocytic sensing of tumor cell-derived antigens triggers the TREM2 program in murine mo-macs, which then promoted the transition of mo-macs toward a pro-tumorigenic state. TREM2$^+$ mo-macs suppress NK cell recruitment and activation by disabling IL-18 signaling and modulating IL-15 production by tumor-infiltrating dendritic cells. Notably, TREM2 blockade unleashed NK cell immunity and significantly eliminated tumors. Finally, we show that combining TREM2 blockade with an NK cell-activating agent yields an even greater antitumor immune response, thus framing a new therapeutic design with high translational potential.

Results

NK cells poorly infiltrate NSCLC lesions unlike TREM2$^+$ mo-macs

We previously generated a large single-cell RNA-sequencing (scRNA-seq) dataset of immune cells from resected tumor lesions and patient-matched, non-involved lung tissues of a cohort of 35 treatment-naive patients with NSCLC[13]. From this atlas, we found that NSCLC lesions are significantly deprived of NK cells, compared to non-involved, adjacent lung tissue (nLung) (Fig. 1a); instead, they are heavily enriched with mo-macs (Fig. 1a) that are transcriptomically distinct from the pool of tissue-resident alveolar macs (AMs), which were preferentially enriched in nLung[13]. Accordingly, the frequency of intratumoral NK cells was inversely correlated with the frequency of mo-macs ($R^2 = 0.0397$, P value = 0.0063), but not with AMs, indicating a potential role for mo-macs, among tumor-enriched mononuclear phagocytes (MNPs)[13], in contributing to the relative absence of NK cells in the TME (Fig. 1b).

To better characterize mo-macs in the TME, we computed differentially expressed genes that distinguished them from AMs; these included *TREM2*, *GPNMB*, *SPP1*, *CTSB*, *RNASE1* and *GPR183* (Fig. 1c and Supplementary Table 1). While no lymphoid cells express *TREM2* (ref. 32), the latent expression of the *TREM2* signature genes by AMs in human NSCLC may indicate that intratumoral cues that induce this signature in recruited mo-macs can also impact the phenotype of the local AM population that otherwise expresses negligible levels of *TREM2* at the steady-state[32] (Fig. 1d). The converse (the potential induction of AM gene programs in recruited mo-macs) may also be probable; however, the de-enrichment of AMs from the intratumoral terrain of the TME and the lack of AM-specific genes (for example, *MARCO*, *PPARG*, *AXL* and *IL18*) expressed by mo-macs, indicate that microenvironmental cues may favor the former scenario, in which tumor-derived signals trigger mo-mac-descriptive gene programs, like the TREM2 program (Supplementary Table 1). Gene set enrichment analysis of the TREM2 program identified active signaling pathways, such as IL-18 signaling, IL-1 signaling and phagocytic vesicle formation, which underscored a unique efferocytic state in mo-macs (Fig. 1e). We confirmed the presence of these TREM2$^+$ macrophages in human NSCLC lesions by immunohistochemical (IHC) co-staining of TREM2 and CD68 proteins (Fig. 1f), motivating us to dissect this signature further to understand how it may modulate the composition and immuno-phenotype of the TME.

Efferocytosis of cell debris induces the TREM2 program in mo-macs

Our group previously published single-cell transcriptomic profiles of MNPs in a murine model of lung cancer[19]. Homology analysis of gene expression across murine and human macrophage clusters showed that analogous TREM2$^+$ mo-macs are significantly enriched in tumor-bearing lungs, relative to naive lungs[19]. To study the dynamic of this population and its functional contribution to antitumor immunity, we leveraged the same orthotopic model of primary lung adenocarcinoma[31], by injecting GFP-expressing KP cells (KP-GFP) to use GFP as a surrogate tumor antigen and track the localization of TREM2$^+$ cells, with respect to GFP$^+$ cells. By confocal microscopy, we found that TREM2$^+$ cells progressively accumulate within growing KP-GFP lung tumors over a 28-d period (Fig. 2a), resembling the intratumoral enrichment that we observed in human NSCLC.

TREM2 has been shown to recognize a variety of ligands and signals via the DAP12 adaptor protein[33,34]. Given that it has also been shown to sense phosphatidylserine on dying cells[35–41], we hypothesized that either the uptake or phagocytic sensing of apoptotic tumor cells may induce the TREM2 program. Confocal imaging of TREM2$^+$ cells showed that many of these phagocytes indeed display intracellular tumor-associated GFP signal (Fig. 2a), supporting our hypothesis that efferocytosis is associated with the expression of TREM2 (Fig. 2a).

To test this hypothesis, we sought to characterize the GFP$^-$ and GFP$^+$ subsets of mo-macs. We purified mo-macs from tumor-bearing lungs and profiled them using bulk RNA-sequencing. From digested tumor-bearing lungs, the intracellular intensity of GFP in mo-macs was not discretely positive or negative, as these cells are likely actively engaged in antigen uptake and digestion upon entering the TME; so instead, we sorted GFP^{lo} and GFP^{hi} mo-macs (Extended Data Fig. 1a). Sequencing these mo-mac subsets showed that efferocytosis of antigens induces significant changes to the transcriptome (Fig. 2b and Supplementary Table 3). Significant differentially expressed genes included hallmark genes belonging to the TREM2 gene program (for example, *Trem2*, *Lpl*, *Syngr1* and *Apoe*). Notably, genes more highly expressed by GFP^{lo} mo-macs included co-stimulatory ligands, MHC class II molecules and cytokines and chemokines critical for the recruitment and activation of CD8$^+$ T cells (*Cd40*, *Il15*, *Il12b*, *Cx3cl1* and *Ccl5*) (Fig. 2b). In contrast, GFP^{hi} mo-macs expressed higher levels of inhibitory genes, including *Cd274*, which encodes PD-L1 (Fig. 2b), lipid metabolism genes (*Apoe*, *Lipa*, *Plin2*, *Lpl* and *Hilpda*), genes involved in antigen uptake and trafficking (*Lrp12*, *Rab7*, *Vat1* and *Mfge8*) and genes encoding machinery proteins for degrading phagocytosed

https://doi.org/10.1038/s41590-023-01475-4

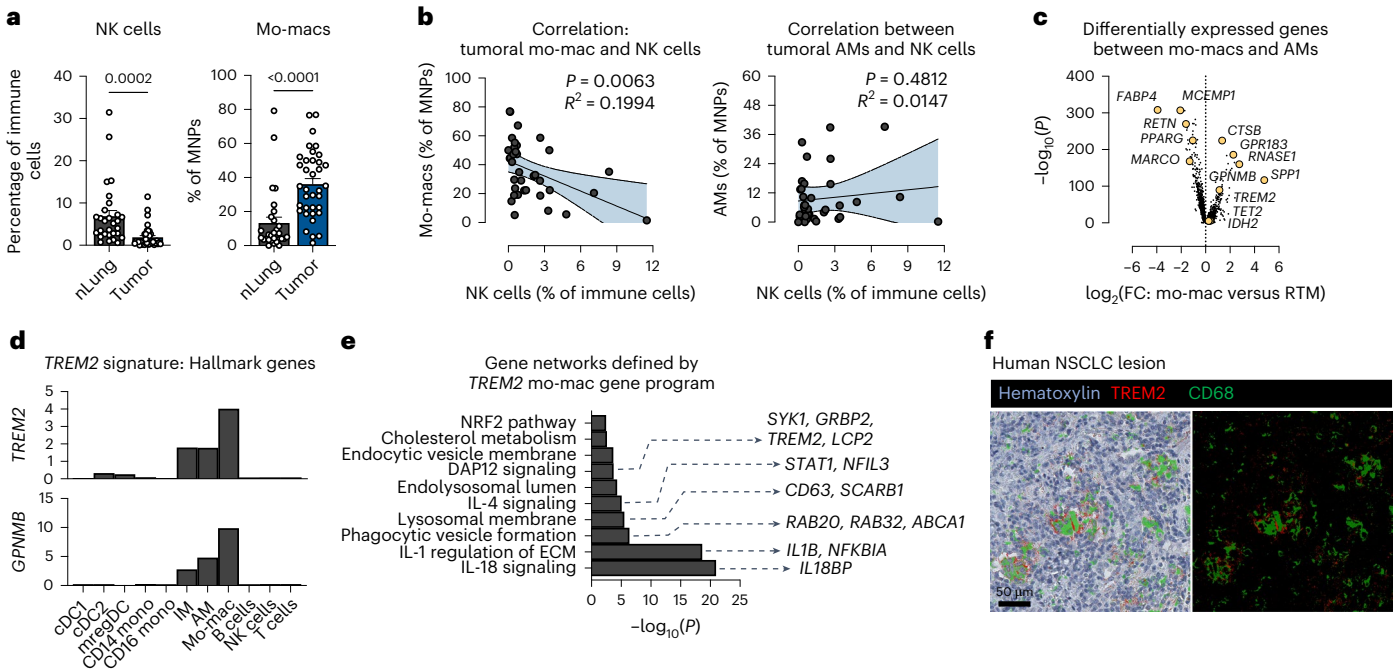

Fig. 1 | TREM2$^+$ monocyte-derived macrophages are major constituents of an NK cell-deprived microenvironment. a, Cell frequency of NK cells identified by scRNA-seq profiling as a percentage of immune cells (left) and the cell frequency of mo-macs as a percentage of MNPs (right) in resected tumors (tumor) and patient-matched nLung from human NSCLC samples from 35 patients with NSCLC (mean ± s.e.m.; unpaired two-tailed *t*-test at 95% CI). **b**, Correlation between the frequency of tumor-infiltrating mo-macs (left) or AMs (right) and of intratumoral NK cells per matched patient sample pair. Linear regression is shown (Pearson correlation test was performed at 95% CI). **c**, Identification of the TREM2 gene program as a universal mo-mac cell state among differentially expressed genes that distinguish mo-macs from AMs using a nonparametric Wilcoxon rank-sum test. **d**, Expression of hallmark TREM2 program genes, showing specificity to mo-macs in the tumor microenvironment, relative to other immune cells identified by scRNA-seq. **e**, Gene set enrichment analysis of gene networks that form among expressed genes in the TREM2 program from **c** using the Enrichr database. **f**, Multiplex immunohistochemistry (mIHC) of a human NSCLC lesion for TREM2 (red) and CD68 (green), shown with hematoxylin counterstain (left) and on a black negative background (right). Scale bar, 50 µm. Image is representative of eight patient samples.

cargo (*Ctsb*, *Ctsd* and *Ctss*) (Fig. 2c). Pathways governing these genes included oxidative phosphorylation, fatty acid metabolism and lysosomal degradation (Extended Data Fig. 1b), whereas pathways active in GFP^{lo} mo-macs are immunogenic (Extended Data Fig. 1b), concordant with the list of differentially expressed genes (Fig. 2b). Notably, significant changes were also observed for cholesterol metabolism genes encoding transporters (*Ldlr*), traffickers (*Npc1*) and packagers (*Plin2*), indicating that potential subcellular changes seen during the acquisition of the TREM2 gene program include cholesterol trafficking (Fig. 2d). Notably, GFP^{hi} mo-macs also downregulated their expression of *Gpr183* and *Marcksl1* (refs. 42,43), suggesting that upon acquiring the TREM2 program, these phagocytes suppress their response to migratory cues that initially recruited them to the TME (Fig. 2e)[44]. Consistent with our ex vivo results, in vitro GFP$^+$ mo-macs (mo-macs cultured with apoptotic tumor cells) upregulated the *Trem2* signature genes, compared to GFP$^-$ mo-macs (control cells) by qPCR (Fig. 2f). Altogether, our results identify efferocytosis as a trigger of the TREM2 program that critically limits the cell-intrinsic immunogenicity of mo-macs.

TREM2 promotes a pro-tumorigenic mo-mac state

To probe the role of TREM2 signaling in tumor-infiltrating mo-macs, we challenged wild-type (WT) and *Trem2*$^{-/-}$ (KO) mice with KP-GFP tumor cells and assessed survival and tumor burden in the lungs at 21 and 28 d after inoculation. KO mice exhibited significantly improved survival and histological quantification of lung tumors showed a notable reduction of tumor burden in KO mice, compared to WT littermates, as early as 21 d after inoculation (Fig. 3a,b). scRNA-seq and flow cytometry of tumor-associated MNPs identified tissue-resident AMs, mo-macs, inflammatory (Ly6C^{hi} and *Ly6c2*-expressing) and patrolling (Ly6C^{lo} and *Ly6c2*-non-expressing) monocytes and conventional dendritic cells (cDCs), including type I cDCs (cDC1s), type II cDCs (cDC2s) and mature cDCs (mregDCs). Tumor-bearing lungs of KO mice were more enriched with AMs and inflammatory monocytes, while exhibiting an attrition of *Trem2*-expressing mo-macs (Fig. 3c–e). Of note, cDC1 were enriched in frequency and absolute numbers in KO mice (Fig. 3c,f), reflecting a preferential enrichment for more cDCs with potent cross-presentation potential in KO mice. Given that *Trem2* expression is not detected in other MNPs, including the cDCs (Extended Data Fig. 2a), we surmised that shifts in the cDC pool from the tumor-bearing lungs of KO mice likely reflect the activity of TREM2-deficient mo-macs.

Alternatively, we considered the possibility that the snapshots of the MNP compartment shown by scRNA-seq were a result of reduced tumor growth. To account for this, we generated bone-marrow chimeric mice by reconstituting sublethally irradiated CD45.1 WT recipient mice with either (1) CD45.1 WT marrow ('WT'); (2) CD45.2 *Trem2*$^{-/-}$ marrow ('KO'); or (3) a 1:1 mixture of both genotypes ('Chimera'), so that in tumor-challenged chimeric mice, both TREM2-proficient and TREM2-deficient cells are exposed to the same TME, allowing us to control for the differences in tumor burden that we previously observed. As expected, KO mice exhibited significantly reduced tumor burden, relative to WT mice. Of note, chimeric mice exhibited an 'intermediate' phenotype, suggesting that the relative abundance of mo-macs highly enriched for the *Trem2* signature drives tumor progression (Fig. 3g). In the chimeric mice, we observed no differences in the frequency of GFP$^+$ cells among mo-macs (Extended Data Fig. 2b,c), indicating that additional means of uptake may be present.

https://doi.org/10.1038/s41590-023-01475-4

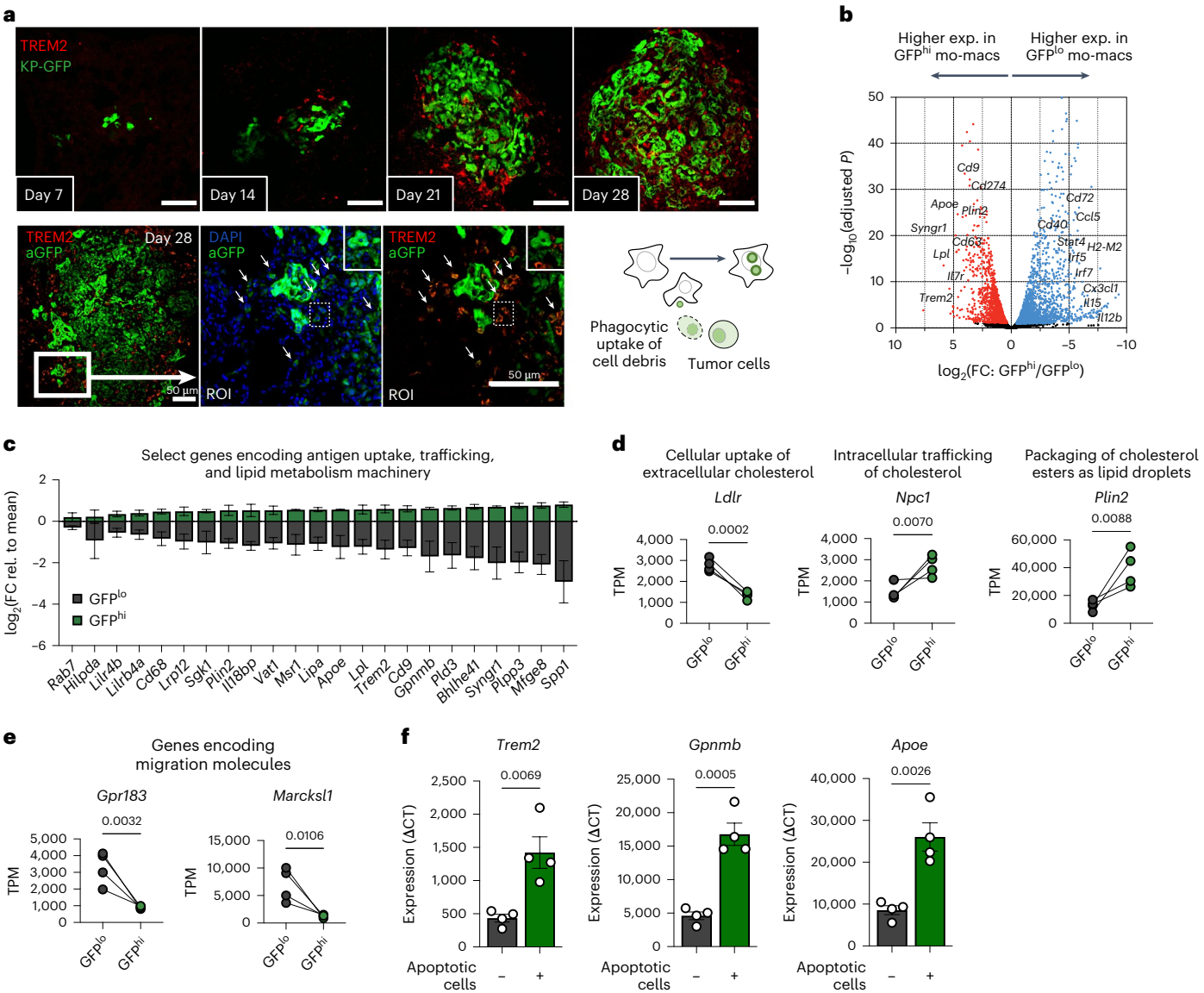

Fig. 2 | Uptake of cellular debris induces the TREM2 gene program in mo-macs. a, Confocal immunofluorescence (IF) imaging of murine KP-GFP tumor-bearing lungs depicting GFP$^+$ tumor cells (green) and TREM2$^+$ cells (red) at different time points during tumor progression (day 7, 14, 21 and 28 after inoculation) (top). Confocal IF imaging of KP-GFP tumor-bearing lungs after 28 d of engraftment and growth (bottom left). Nuclei, 4,6-diamidino-2-phenylindole (DAPI); GFP, green; TREM2, red. Scale bar, 50 µm. Pictorial diagram showing relationship between efferocytosis and TREM2 (bottom, right). Images are representative of three independent experiments. **b**, Volcano plot of differentially expressed genes between GFP^{lo} and GFP^{hi} mo-macs. Statistical significance defined based on an adjusted $P < 0.01$ based on a negative binomial distribution and using an estimation for variance–mean dependence. Significant genes are highlighted in either red (upregulated upon tumor antigen capture) or blue (downregulated upon tumor antigen capture). Data are representative of two independent experiments. **c**, Expression of *Trem2* signature genes and other select genes encoding machinery involved in phagocytosed cargo transport, antigen processing and lipid metabolism by GFP^{lo} and GFP^{hi} mo-macs. Values shown as the logarithm of fold change of absolute number of transcripts relative to the mean value across replicates ($n = 3$ mice, mean ± s.e.m.). **d**, Absolute expression (TPM) of genes encoding LDL receptor, NPC1 and PLIN2 in GFP^{lo} and GFP^{hi} mo-macs. Paired values shown for paired GFP^{lo} and GFP^{hi} mo-macs that were purified from the same biological replicate. Data from two independent experiments. (mean ± s.e.m.; unpaired two-tailed *t*-test at a 95% CI). TPM, transcripts per million. **e**, Absolute expression (TPM) of genes encoding GPR183 and MARCKSL1 in GFP^{lo} and GFP^{hi} mo-macs. Paired values shown for paired GFP^{lo} and GFP^{hi} mo-macs that were purified from the same biological replicate. Data are from two independent experiments (mean ± s.e.m.; unpaired two-tailed *t*-test at a 95% CI). **f**, Relative qPCR quantification of *Trem2*, *Gpnmb* and *Apoe* transcripts from in vitro differentiated bone-marrow-derived macrophages (BMDMs) with or without (control) exposure to apoptotic KP-GFP cells. Transcripts are shown as the twofold difference in gene expression (ΔCt) over *Ptprc* expression ($n = 4$ replicates, mean TPM ± s.e.m.; unpaired two-tailed *t*-test at a 95% CI). Data shown are representative of two independent experiments.

To assess cell-intrinsic differences between CD45.1 WT and CD45.2 KO phagocytes, we performed scRNA-seq of purified CD45.1 WT and CD45.2 KO MNPs from the tumor-bearing lungs of the chimeric mice. Unsupervised clustering identified a mix of CD45.1 and CD45.2 mo-macs in the TME of chimeric mice; however, examination of the expression of genes belonging to the TREM2 gene program (*Gpnmb*, *Spp1*, *Lipa*, *Lpl*, *Plin2*, *Fabp5*, *Syngr1*, *Gpr183*, *Cd9*, *Sgk1*, *Apoe*, *Mfge8*, *Il18bp* and *Lilrb4a*), with the exception of *Trem2* itself, enabled us to describe the role of TREM2 in the transcriptomic architecture of mo-macs in a tumor-burden-controlled setting (Fig. 3h). We could partition mo-macs into those highly enriched for the expression of the aforementioned genes, in which case we denoted these cells as those

https://doi.org/10.1038/s41590-023-01475-4

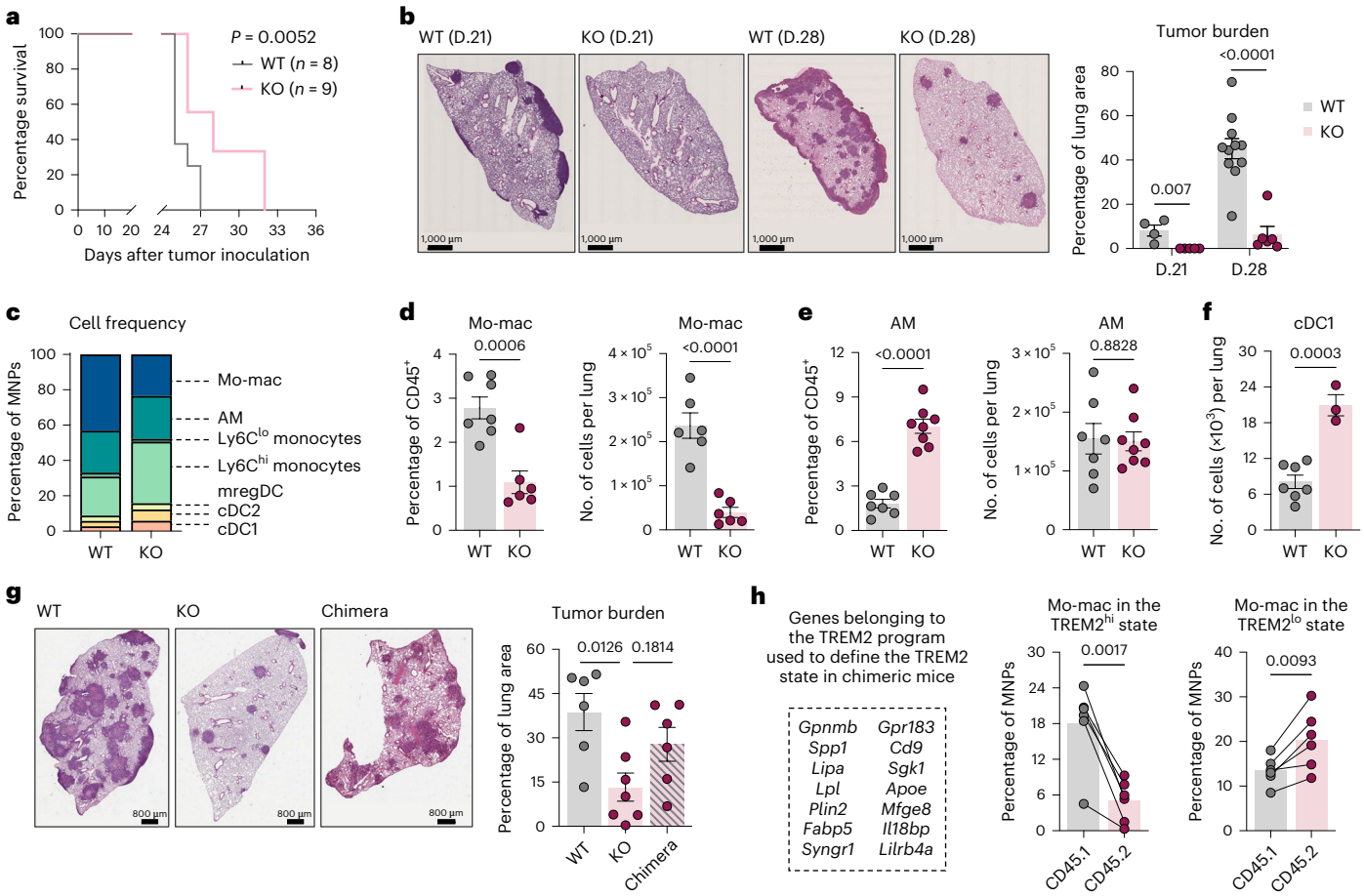

Fig. 3 | TREM2 deficiency restricts tumor growth by remodeling the composition of MNPs. a, Kaplan–Meier survival curve of KP-GFP tumor-bearing WT ($n = 8$) and KO ($n = 9$) mice. Statistics computed using the log-rank test. **b**, Representative hematoxylin and eosin (H&E) images of tumor-bearing lungs of WT and KO mice at day 21 (WT, $n = 4$; KO, $n = 4$) and at day 28 (WT, $n = 11$; KO, $n = 6$) after inoculation of tumor cells (left). Quantification of the tumor area as a percent of the total area of the lung cross-section (right) is shown. Data are representative of three independent experiments (mean ± s.e.m.; multiple unpaired two-sampled *t*-tests). **c**, Cell frequency changes of MNPs based on scRNA-seq profiling of WT ($n = 2$) and KO ($n = 2$) mice. Frequencies for each group are shown as the mean of each pair of duplicates. **d**, Flow cytometric quantification of mo-macs, represented as relative frequency among CD45$^+$ immune cells (left) and as absolute number of cells per lung (right) from tumor-bearing lungs of WT and KO mice at day 28 after inoculation ($n = 6$–8 mice per group, mean ± s.e.m.; unpaired two-tailed *t*-test at 95% CI). Data shown are representative of five independent experiments. **e**, Flow cytometric quantification of AMs, represented as relative frequency among CD45$^+$ immune cells (left) and as the absolute number of cells per lung (right), from tumor-bearing lungs of WT and KO mice at day 28 after inoculation. The results shown are from one experiment, representative of five independent experiments ($n = 6$–8 mice per group, mean ± s.e.m.; unpaired two-tailed *t*-test at a 95% confidence interval). Data shown are representative of five independent experiments. **f**, Flow cytometric quantification of cDC1, represented as the absolute number of cells per lung from tumor-bearing lungs of WT and KO mice at day 28 after inoculation of tumor cells ($n = 4$–7 mice per group, mean ± s.e.m.; unpaired two-tailed *t*-test at a 95% CI). Data shown are representative of two separate, independent experiments. **g**, Representative H&E images of tumor-bearing lungs of WT, KO and chimeric mice (left) at day 28 after tumor cell inoculation (left) and quantification of the tumor area as a percent of the total area of the lung cross-section (right) is shown (mean ± s.e.m.; unpaired two-tailed *t*-test at 95% CI). **h**, Genes of the TREM2 gene program whose expression defines the TREM2 cell state (left). Frequencies of mo-macs in the TREM2^{hi} and TREM2^{lo} cell states, represented as a relative frequency among MNPs from the purified CD45.1 WT and CD45.2 KO fractions of MNPs from KP-GFP tumor-bearing chimeric mice. Paired values shown for paired CD45.1 WT and CD45.2 KO cells that were purified from the same biological replicate ($n = 6$ mice, mean ± s.e.m.; paired two-tailed *t*-test at 95% CI).

in the TREM2^{hi} state, whereas those lowly enriched for the expression of these genes were annotated as cells in a TREM2^{lo} state. Notably, mo-macs in the TREM2^{hi} state were dominantly represented by CD45.1 WT cells, whereas mo-macs in the TREM2^{lo} state were more significantly represented by CD45.2 KO cells (Fig. 3h), suggesting that the expression of TREM2 acts as a master regulator of the broader TREM2 gene program and that its genetic deletion interrupts the molecular transition of mo-macs toward a pro-tumorigenic state. Notably, given that monocytes do not express *Trem2* and that TREM2 is expressed once monocytes differentiate into mo-macs in tumor lesions (Extended Data Fig. 2a), there may be a temporal element to the acquisition of and enrichment for the TREM2 program that is initially coupled to the degree of efferocytic sensing. Collectively, our results highlight a crucial, cell-intrinsic role for TREM2 in governing the mo-mac transition toward the TREM2^{hi} state, which we find has major consequences for antitumor immunity.

TREM2$^+$ mo-macs restrict NK-cell-mediated antitumor immunity

Flow cytometry of T cells revealed a marked expansion of antigen-specific, polyfunctional CD8$^+$ T cells in the tumor-bearing lungs and tumor-draining lymph nodes (tdLNs) of KO mice challenged with OVA-expressing KP-GFP cells (KP-GFP-OVA), compared to WT mice (Fig. 4a and Extended Data Fig. 3a). We also observed an

https://doi.org/10.1038/s41590-023-01475-4

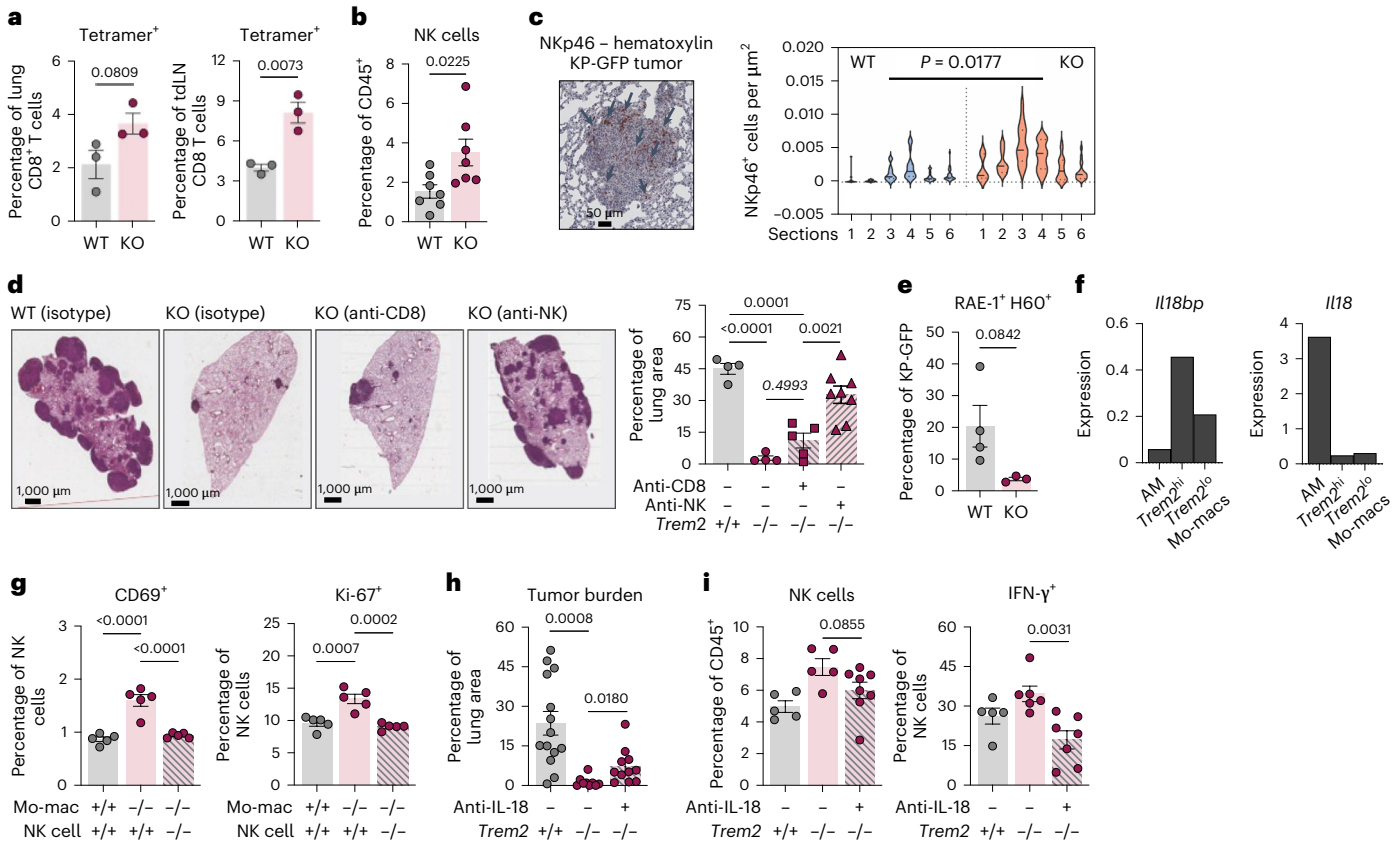

Fig. 4 | Therapeutic effect of TREM2 deficiency is critically dependent on intact IL-18 and IL-15 signaling. a, Flow cytometric quantification of OVA-tetramer$^+$ (antigen-specific) CD8$^+$ T cells, represented as the relative frequency among total CD8$^+$ T cells in the lungs (left) and tdLNs (right) of KP-GFP-OVA tumor-bearing WT and KO mice ($n = 3$ mice per group, mean ± s.e.m.; unpaired two-tailed t-test at 95% CI). Data shown are representative of at least two independent experiments. **b**, Flow cytometric quantification of NK cells, represented as the relative frequency of CD45$^+$ immune cells (left) and as absolute number of cells per lung (right) in the KP-GFP tumor-bearing lungs of WT and KO mice ($n = 3$ mice per group, mean ± s.e.m.; unpaired two-tailed t-test at 95% CI). Data shown are representative of at least two independent experiments. **c**, Representative IHC staining of NKp46 for NK cells in a KP-GFP tumor from a KO mouse (left). Arrows mark positively stained cells. Quantification of NKp46$^+$ cells in a representative tissue section per lung sample from WT ($n = 6$) and KO ($n = 6$) mice (right). **d**, Representative H&E images of tumor-bearing lungs of WT, isotype antibody ($n = 4$), KO, isotype antibody ($n = 4$), KO mice depleted of CD8$^+$ T cells (KO + anti-CD8, $n = 5$), KO mice depleted of NK cells (KO + anti-NK, $n = 8$) at day 28 after inoculation of tumor cells (left). Quantification of the tumor area as a percent of the total area of the lung cross-section (right) is shown (mean ± s.e.m.; unpaired two-tailed t-test at 95% CI). **e**, Flow cytometric quantification of RAE-1$^+$H60$^+$ tumor cells, as a relative frequency of total KP-GFP tumor cells, in the tumor-bearing lungs of WT and KO mice ($n = 4$ WT mice and 3 KO mice, mean ± s.e.m.; unpaired two-tailed t-test at 95% CI). **f**, Expression of the *Il18bp* (left) and *Il18* (right) transcripts, as defined as the mean number of unique molecular identifiers (UMIs), by AMs, *Trem2*^{hi} mo-macs and *Trem2*^{lo} mo-macs, as identified by unsupervised clustering of scRNA-seq profiling of MNPs in KP-GFP tumor-bearing WT and KO mice. **g**, Flow cytometric quantification of CD69$^+$ activated NK cells (left) and of Ki-67$^+$ proliferative NK cells (right), shown as a frequency of total NK cells. The results shown are from one experiment, representative of three independent experiments (mean ± s.e.m.; unpaired two-tailed t-test at 95% CI). **h**, Quantification of the tumor area, as a percent of the total area of the lung cross-section, of tumor-bearing lungs of WT, isotype antibody ($n = 6$), KO, isotype antibody ($n = 6$) and KO mice that received the IL-18 neutralizing antibody ($n = 8$). The results shown are from two independent experiment ($n = 5$–8 mice per group, mean ± s.e.m.; unpaired two-tailed t-test at 95% CI). Data shown are representative of three independent experiments. **i**, Flow cytometric quantification of NK cells, as a relative frequency of CD45$^+$ immune cells (left) and of IFN-γ-producing NK cells, as a relative frequency among total NK cells (right) ($n = 5$–8 mice per group, mean ± s.e.m.; unpaired two-tailed t-test at 95% CI). Data shown are representative of at least three independent experiments.

expansion of NK cells that were significantly more activated and cytolytic in KO mice (Fig. 4b and Extended Data Fig. 3b); multiplex imaging also indicated that, in the absence of functional TREM2, NK cells accumulate within tumors, indicating a spatially relevant increase in the NK cell content of tumor-bearing lungs in KO mice (Fig. 4c).

Of note, while depleting CD8$^+$ T cells only partially reversed the decrease in tumor burden in tumor-bearing KO mice, NK cell depletion completely abrogated the tumor reduction phenotype (Fig. 4d). Moreover, only NK cell depletion reversed the expansion of cDC1 in KO mice (Extended Data Fig. 3c). Indeed, in tumor-bearing WT and KO mice deprived of NK cells, the NK cell-dependent reduction of tumor burden could only be observed in the KO mice, suggesting that the significance of the NK cell response to KP-GFP lung tumors is only realized in the absence of functional TREM2$^+$ mo-macs (Extended Data Fig. 3d,e). In line with these results, we found a reduction in the proportion of KP-GFP tumor cells that express NKG2D ligands (RAE-1 and H60) in KO mice, compared to WT mice, reflecting the NK cell-driven elimination of tumor cells that is enabled by TREM2 deficiency (Fig. 4e). For these reasons, we postulated that TREM2$^+$ mo-macs do indeed play an active role in the paucity and poor cytolytic activity of NK cells in the TME of lung tumors.

We then leveraged the scRNA-seq-based molecular profiles of *Trem2*^{hi} and *Trem2*^{lo} mo-macs of CD45.1 WT and CD45.2 KO MNPs in the lungs of tumor-bearing chimeric mice to identify potential molecules that could impact NK cell recruitment and activation. We found that

https://doi.org/10.1038/s41590-023-01475-4

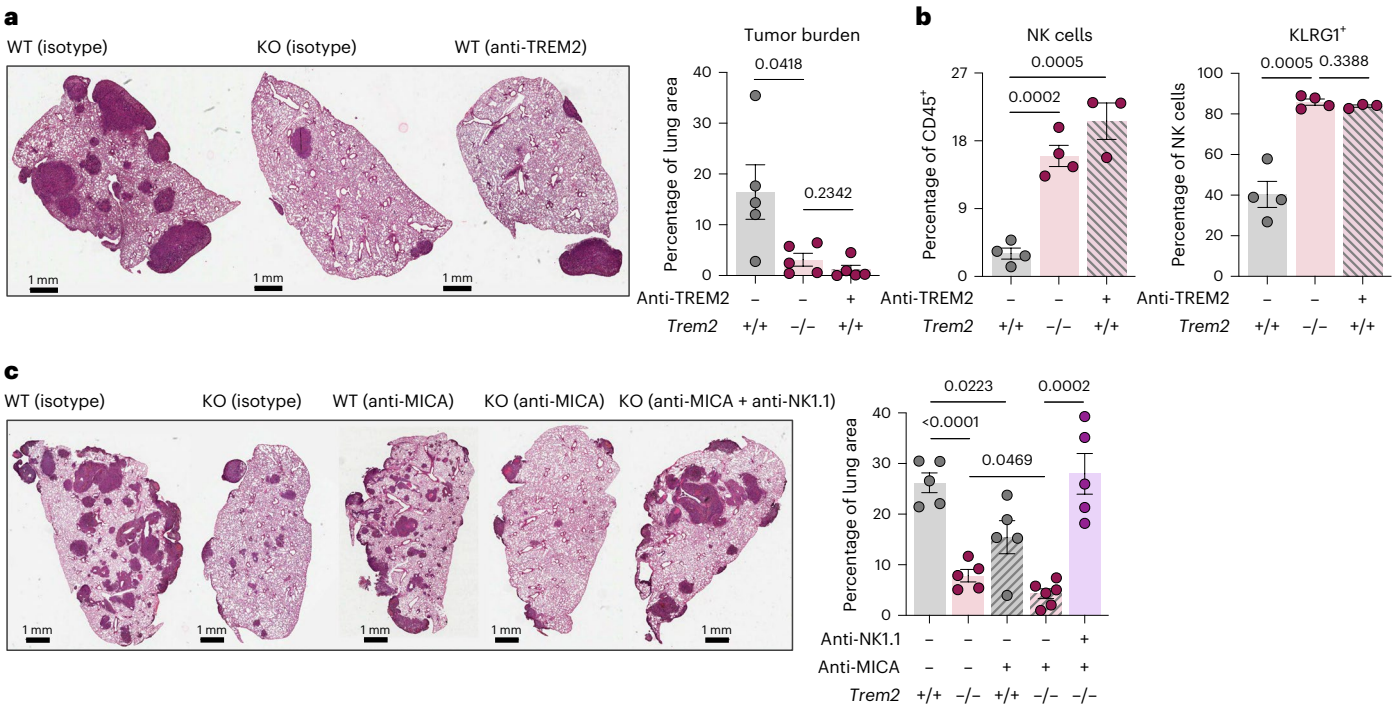

Fig. 5 | Therapeutic inhibition of TREM2 synergizes with an NK-cell-stabilizing agent to promote superior NK cell immunity and tumor elimination. a, Representative H&E images of tumor-bearing lungs of WT, isotype antibody ($n = 5$), KO, isotype antibody ($n = 5$), KO that received the TREM2 blocking antibody (anti-TREM2) ($n = 5$) (left). Quantification of the tumor area as a percent of the total area of the lung cross-section (right) is shown (mean ± s.e.m.; unpaired two-tailed *t*-test at 95% CI). **b**, Flow cytometric quantification of NK cells, as a relative frequency of CD45$^+$ immune cells (left) and KLRG1-expressing NK cells, as a relative frequency of total NK cells (right), in the tumor-bearing lungs of WT mice and KO mice that were treated with either an isotype control or the TREM2 antibody ($n = 3$–4 mice per group, mean ± s.e.m.; unpaired two-tailed *t*-test at 95% CI). Data shown are representative of at least two independent experiments. **c**, Representative H&E images of tumor-bearing lungs of WT, isotype antibody ($n = 5$), KO, isotype antibody ($n = 5$), WT that received the MIC-A stabilizing antibody (anti-MICA) ($n = 5$), KO that received the anti-MICA ($n = 6$) and KO that received both anti-MICA and an NK cell-depleting antibody ($n = 5$) (left). Quantification of the tumor area as a percent of the total area of the lung cross-section from tumor-bearing lungs of these mice is shown (right) (mean ± s.e.m. unpaired two-tailed *t*-test at 95% CI).

Trem2^{hi} mo-macs express uniquely high levels of *Il18bp*, compared to *Trem2*^{lo} mo-macs and AM (Fig. 4f). The *Il18bp* gene encodes the decoy protein IL-18BP that intercepts IL-18 and prevents signaling in cells expressing the IL-18 receptor[45,46]. AM are the main expressors of *Il18* (Fig. 4f), highlighting the potential role of IL-18 signaling, or rather, the lack thereof possibly due to the reorganization of AM to the peripheral tumor bed[19], in the regulation of NK cells by TREM2$^+$ mo-macs. These results aligned with the network analysis of human TREM2$^+$ mo-macs (Fig. 1e).

To functionally test this, we leveraged an in vitro coculture assay, where we generated mo-macs from WT and KO mice and cultured them with splenic NK cells from WT and *Il18r1* knockout mice that were stimulated with IL-18 and IL-12. We assessed NK cell activation based on the expression of the activation marker CD69 and proliferative potential (expression of Ki-67); the absence of TREM2 on mo-macs significantly enhanced the activation of NK cells, which was abrogated in the absence of the IL-18 receptor on NK cells (Fig. 4g), indicative of the possible role of secreted IL-18BP in interfering with the available IL-18 that we introduced to the coculture. Moreover, as IL-12 was included in the stimulus cocktail for all conditions, the significant decline in response, in the absence of the IL-18 receptor on NK cells, suggested that IL-12 alone, though it may still contribute to the shaping of the CD8$^+$ T cell response, likely does not play a major role in the regulation of NK cells by TREM2$^+$ mo-macs. Notably, IL-18 blockade in KO mice partially reversed the tumor reduction phenotype, compared to untreated KO mice (Fig. 4h); it also tampered with the recruitment and activation of NK cells and the activation of CD8$^+$ T cells (Fig. 4i and Extended Data Fig. 3f), suggesting that IL-18 signaling contributes to the activation of NK cells that is suppressed by TREM2 on mo-macs.

IL-18 is well known to require cooperative signaling with cytokines expressed by cDCs, such as the trans-presented cytokine IL-15, to enhance and sustain the cytolytic NK cell response[47–49]. So, we sought to determine whether the NK cell enhancement in the absence of TREM2 relied upon this example of cooperative cytokine signaling. From our single-cell profiling of MNPs in the tumor-bearing lungs of WT and KO mice, we documented an upregulation of the *Il15* transcript by the mature mregDCs in KO mice (Extended Data Fig. 4a). Therefore, we chose to examine the role of IL-15 in the tumor reduction phenotype in KO mice. We blocked IL-15 in tumor-bearing KO mice, using an IL-15 neutralizing antibody, to determine whether IL-15 signaling itself is an essential component of the TREM2$^+$ mo-mac/NK cell mechanism. IL-15 blockade completely abrogated both the tumor reduction phenotype and expansion of NK cells in KO lungs (Extended Data Fig. 4b,c), suggesting that upon expansion of cDC1s into the TME of KO mice, IL-15 is needed to sustain the NK cell response.

Dual targeting of TREM2 and NK cells as a new therapy

To evaluate the therapeutic and translational potential of targeting TREM2$^+$ mo-macs in the lung TME, we tested a non-depleting TREM2 blocking antibody (anti-TREM2) in KP-GFP-challenged WT mice, as previously described[27]. Treatment resulted in a strong reduction of tumor growth in WT mice, comparable to the effect observed in KO mice (Fig. 5a). The recruitment and activation of NK cells in anti-TREM2-treated mice was also comparable to those in the tumor-bearing lungs of KO mice (Fig. 5b). We reasoned that leveraging strategies to boost any feature of NK cell immunity could enhance the antitumor effect of TREM2 blockade, so we assessed a dual-targeting approach using the

anti-TREM2 blocking antibody with agents that release the breaks on NK cell activation, by preventing the degradation of NK cell-activating ligands. The human MHC class I polypeptide-related sequence A (MIC-A), for example, is an activating ligand that interacts with NKG2D on NK cells and relays a positive signal that boosts NK cell-derived interferon (IFN)-γ production and the release of granzymes; however, while MIC-A expression is conserved across many human tumors, these lesions are able to escape NK cell recognition by cleaving MIC-A with ADAMs/MMPs and shedding it from the surface[50]. We recently found that an antibody that stabilizes MIC-A by shielding the extracellular domains from proteolytic cleavage can serve as a promising NK cell-based immunotherapeutic[50]. Therefore, we explored its synergistic potential in combination with TREM2 deficiency by challenging WT and KO mice with the metastatic melanoma B16-F10 cell line, which is engineered to express MIC-A (B16-F10-MICA). Treatment with the MIC-A stabilizing antibody (anti-MICA) significantly reduced metastatic lesions in the lungs of KO mice, compared to WT mice, highlighting a synergy between both TREM2 deficiency and the stabilization of NK cell activation in vivo. In addition, the therapeutic effect of the combination treatment was completely abrogated by NK cell depletion (Fig. 5c), supporting a robust axis of immunity between TREM2$^+$ mo-macs and NK cells that oversees the lung environment, whether that be in response to primary lung tumors or metastatic melanoma lesions in the lungs.

Discussion

A scarcity of intratumoral cytolytic NK cells is a feature of the TME, not just in NSCLC but in many other cancer types[51–54], suggesting that the depletion of NK cells enables tumor growth. Yet, identifying the cellular networks behind this 'NK cell desert' phenotype in the tumor topography has continued to be a major obstacle. Unleashing NK cell-mediated elimination of target tumor cells provides the advantage of occurring independently of the repertoire of tumor antigens; therefore, this could still eliminate tumors that escaped T cell surveillance. In the present study, we report that among the various MNPs that instruct effector cell activity, the pool of mo-macs expressing TREM2 is uniquely abundant in tumor lesions and inversely correlated in frequency with that of NK cells, prompting us to explore whether they help disable NK cell recruitment and activation in NSCLC lesions. We leveraged scRNA-seq of human and murine NSCLC to show that murine TREM2$^+$ mo-macs, like their homologous human counterparts, accumulate with tumor growth and efficiently infiltrate lesions, unlike the tissue-resident AMs[19]. Of note, in contrast to the expression of *TREM2* signature genes by AMs, albeit to a lower extent than mo-macs, in human NSCLC, the lack of AM genes (*MARCO*, *PPARG* and *FABP4*) expressed by mo-macs may suggest that the homeostatic signals that otherwise promote 'proper' differentiation of tissue-infiltrating monocyte-derived cells into AMs do not seem to promote the AM program in recruited macrophages during tumorigenesis[18]. This particular difference emphasizes both the lack of homeostatic cues due to the loss of niche integrity and supports the ontogenic distinction between AMs and mo-macs in lung tumors, as we previously demonstrated by fate-mapping MNPs in murine lung tumors[19,20].

TREM2$^+$ mo-macs exhibited significant intracellular GFP signal, captured from KP-GFP tumor cells, but at comparable levels to TREM2-deficient mo-macs, indicating two notable features about the biology of the TREM2 program in these cells: first, the TREM2-deficient phagocytes remain able to capture tumor cell-derived antigens and second, given that the rate of GFP uptake is similar between TREM2-proficient and TREM2-deficient mo-macs, it is likely that sensing and not necessarily the physical uptake, of these materials induces the TREM2 program. Notably, the acquisition of the TREM2 program by mo-macs mutes pro-inflammatory pathways by downregulating co-stimulation genes and upregulating those encoding immune-checkpoint molecules. The identification of lipid metabolism pathways based on program-specific genes and specific changes in the expression of genes encoding cholesterol-trafficking machinery prompted us to describe these mo-macs enriched in the TREM2 program as having entered a dysfunctional cholesterolemic state, but the extent to which we further investigate their subcellular properties will be the focus of future studies. We suspect that TREM2$^+$ mo-macs divert cholesterol to excess lipid droplets, which have been shown to have immunoregulatory properties associated with the resource partitioning of free cholesterol via apolipoprotein E (encoded by *Apoe*), suppression of antigen presentation and response to IFN in cDC1s (refs. 55,56). But additional work will still be necessary to fully understand how this lipidic state regulates the immunoregulatory potential of intratumoral TREM2$^+$ mo-macs[57]. Recent molecular work suggests that tumor cell-derived glucosyl-ceramide stimulates a reshuffling of lipid composition in macrophages by inducing cholesterol imbalance and promoting ER stress, both of which result in the expression of XBP1. Deleting the *Xbp1* gene in intratumoral macrophages reversed this phenotype and restrained growth of subcutaneous melanoma lesions[58]. TREM2 itself has also been shown to regulate cholesterol metabolism in microglia[59], so an understanding of how intratumoral TREM2$^+$ mo-macs utilize their intracellular cholesterol depots, in contrast to the ways their tissue-resident counterparts may do so, would truly be essential for exploring other methods of skewing the phenotype of these cells.

Genetic ablation of *Trem2* significantly reduced lung tumor burden in both experimental lung adenocarcinoma and in lung metastases of melanoma. Deleting *Trem2* enhanced the expression of *Il18bp*, encoding the decoy protein that intercepts IL-18 and has been shown to suppress antitumor NK cell responses[46]. Notably, as AMs, which mainly localize at the periphery of the tumor, are a source of IL-18 (refs. 60,61), it is possible that the exclusion of NK cells at the tumor bed may reflect their accumulation around an IL-18 source located outside of the tumor.

The absence of TREM2 also led to enhanced NK cell function that was dependent on IL-15, which is highly expressed by mregDCs. While the recruitment of NK cells by mregDCs and their role in antitumor immunity is well appreciated[62–64], it was notable to find that this axis was, in fact, tightly regulated by TREM2$^+$ mo-macs in NSCLC. Altogether, these results position TREM2$^+$ mo-macs as 'bouncers' of the TME, keeping NK cells from effectively killing tumor cells. The enrichment of NK cells and cDC1s has been associated with response to PD-1 blockade in patients with melanoma, so answering whether TREM2$^+$ mo-macs also define response to immune-checkpoint blockade in patients with NSCLC could be additional, powerful evidence that these macrophages should be studied in greater detail in different tissues.

In our report, we demonstrate that combining TREM2 blockade with exogenous NK-cell-enhancing agents does indeed further boost the antitumor response, and this finding highlights a new therapeutic strategy for targeting effector immune cells in the TME without concerns for revitalizing an antigen-specific adaptive immune response that is so heavily dependent on presentation of immunogenic tumor antigens. In summary, we propose that TREM2 on mo-macs is a major immune checkpoint that mutes NK-cell-mediated antitumor immunity in NSCLC. The ability for TREM2$^+$ mo-macs to regulate NK cells provides a strong rationale for the clinical development of combinatorial therapies that concurrently inhibit TREM2 and enhance NK cells, including the anti-MICA stabilizing agent that we used in our study and is currently in clinical trials to manage solid tumors (NCT05117476).

Online content

Any methods, additional references, Nature Portfolio reporting summaries, source data, extended data, supplementary information, acknowledgements, peer review information; details of author contributions and competing interests; and statements of data and code availability are available at https://doi.org/10.1038/s41590-023-01475-4.

References

1. Dunn, G. P., Bruce, A. T., Ikeda, H., Old, L. J. & Schreiber, R. D. Cancer immunoediting: from immunosurveillance to tumor escape. *Nat. Immunol.* **3**, 991–998 (2002).
2. Molgora, M., Cortez, V. S. & Colonna, M. Killing the invaders: NK cell impact in tumors and anti-tumor therapy. *Cancers* **13**, 595 (2021).
3. Gasser, S., Orsulic, S., Brown, E. J. & Raulet, D. H. The DNA damage pathway regulates innate immune system ligands of the NKG2D receptor. *Nature* **436**, 1186–1190 (2005).
4. Raulet, D. H., Gasser, S., Gowen, B. G., Deng, W. & Jung, H. Regulation of ligands for the NKG2D activating receptor. *Annu. Rev. Immunol.* **31**, 413–441 (2013).
5. Hayakawa, Y. & Smyth, M. J. NKG2D and cytotoxic effector function in tumor immune surveillance. *Semin. Immunol.* **18**, 176–185 (2006).
6. Smyth, M. J., Hayakawa, Y., Takeda, K. & Yagita, H. New aspects of natural-killer-cell surveillance and therapy of cancer. *Nat. Rev. Cancer* **2**, 850–861 (2002).
7. Parham, P. & Guethlein, L. A. Genetics of natural killer cells in human health, disease, and survival. *Annu. Rev. Immunol.* **36**, 519–548 (2018).
8. Garrido, F., Aptsiauri, N., Doorduijn, E. M., Garcia Lora, A. M. & van Hall, T. The urgent need to recover MHC class I in cancers for effective immunotherapy. *Curr. Opin. Immunol.* **39**, 44–51 (2016).
9. McGranahan, N. et al. Allele-specific HLA loss and immune escape in lung cancer evolution. *Cell* **171**, 1259–1271 (2017).
10. Cózar, B. et al. Tumor-infiltrating natural killer cells. *Cancer Discov.* **11**, 34–44 (2021).
11. Shimasaki, N., Jain, A. & Campana, D. NK cells for cancer immunotherapy. *Nat. Rev. Drug Discov.* **19**, 200–218 (2020).
12. Lavin, Y. et al. Innate immune landscape in early lung adenocarcinoma by paired single-cell analyses. *Cell* **169**, 750–765 (2017).
13. Leader, A. M. et al. Single-cell analysis of human non-small cell lung cancer lesions refines tumor classification and patient stratification. *Cancer Cell* **39**, 1594–1609 (2021).
14. Mulder, K. et al. Cross-tissue single-cell landscape of human monocytes and macrophages in health and disease. *Immunity* **54**, 1883–1900 (2021).
15. DeNardo, D. G. et al. CD4(+) T cells regulate pulmonary metastasis of mammary carcinomas by enhancing protumor properties of macrophages. *Cancer Cell* **16**, 91–102 (2009).
16. Masetti, M. et al. Lipid-loaded tumor-associated macrophages sustain tumor growth and invasiveness in prostate cancer. *J. Exp. Med.* **219**, e20210564 (2022).
17. Lavin, Y., Mortha, A., Rahman, A. & Merad, M. Regulation of macrophage development and function in peripheral tissues. *Nat. Rev. Immunol.* **15**, 731–744 (2015).
18. Park, M. D., Silvin, A., Ginhoux, F. & Merad, M. Macrophages in health and disease. *Cell* **185**, 4259–4279 (2022).
19. Casanova-Acebes, M. et al. Tissue-resident macrophages provide a pro-tumorigenic niche to early NSCLC cells. *Nature* **595**, 578–584 (2021).
20. Loyher, P.-L. et al. Macrophages of distinct origins contribute to tumor development in the lung. *J. Exp. Med.* **215**, 2536–2553 (2018).
21. Guerreiro, R. et al. TREM2 variants in Alzheimer's disease. *N. Engl. J. Med.* **368**, 117–127 (2013).
22. Sims, R. et al. Rare coding variants in PLCG2, ABI3, and TREM2 implicate microglial-mediated innate immunity in Alzheimer's disease. *Nat. Genet.* **49**, 1373–1384 (2017).
23. Wang, S. et al. Anti-human TREM2 induces microglia proliferation and reduces pathology in an Alzheimer's disease model. *J. Exp. Med.* **217**, e20200785 (2020).
24. Zhou, Y. et al. Human and mouse single-nucleus transcriptomics reveal TREM2-dependent and TREM2-independent cellular responses in Alzheimer's disease. *Nat. Med.* **26**, 131–142 (2020).
25. Binnewies, M. et al. Targeting TREM2 on tumor-associated macrophages enhances immunotherapy. *Cell Rep.* **37**, 109844 (2021).
26. Katzenelenbogen, Y. et al. Coupled scRNA-seq and Intracellular protein activity reveal an immunosuppressive role of TREM2 in cancer. *Cell* **182**, 872–885 (2020).
27. Molgora, M. et al. TREM2 modulation remodels the tumor myeloid landscape enhancing anti-PD-1 immunotherapy. *Cell* **182**, 886–900 (2020).
28. Esparza-Baquer, A. et al. TREM-2 defends the liver against hepatocellular carcinoma through multifactorial protective mechanisms. *Gut* **70**, 1345–1361 (2021).
29. Perugorria, M. J. et al. Non-parenchymal TREM-2 protects the liver from immune-mediated hepatocellular damage. *Gut* **68**, 533–546 (2019).
30. Tang, W. et al. TREM2 acts as a tumor suppressor in hepatocellular carcinoma by targeting the PI3K/Akt/β-catenin pathway. *Oncogenesis* **8**, 9 (2019).
31. DuPage, M., Dooley, A. L. & Jacks, T. Conditional mouse lung cancer models using adenoviral or lentiviral delivery of Cre recombinase. *Nat. Protoc.* **4**, 1064–1072 (2009).
32. Heng, T. S. P. & Painter, M. W. The Immunological Genome Project: networks of gene expression in immune cells. *Nat. Immunol.* **9**, 1091–1094 (2008).
33. Cannon, J. P., O'Driscoll, M. & Litman, G. W. Specific lipid recognition is a general feature of CD300 and TREM molecules. *Immunogenetics* **64**, 39–47 (2012).
34. Daws, M. R. et al. Pattern recognition by TREM-2: binding of anionic ligands. *J. Immunol.* **171**, 594–599 (2003).
35. Filipello, F. et al. The microglial innate immune receptor TREM2 is required for synapse elimination and normal brain connectivity. *Immunity* **48**, 979–991 (2018).
36. Hsieh, C. L. et al. A role for TREM2 ligands in the phagocytosis of apoptotic neuronal cells by microglia. *J. Neurochem.* **109**, 1144–1156 (2009).
37. Iizasa E. et al. TREM2 is a receptor for non-glycosylated mycolic acids of mycobacteria that limits anti-mycobacterial macrophage activation. *Nat. Commun.* **12**, 2299 (2021).
38. Lue, L.-F., Schmitz, C. & Walker, D. G. What happens to microglial TREM2 in Alzheimer's disease: Immunoregulatory turned into immunopathogenic? *Neuroscience* **302**, 138–150 (2015).
39. Shirotani, K. et al. Aminophospholipids are signal-transducing TREM2 ligands on apoptotic cells. *Sci. Rep.* **9**, 7508 (2019).
40. Takahashi, K., Rochford, C. D. P. & Neumann, H. Clearance of apoptotic neurons without inflammation by microglial triggering receptor expressed on myeloid cells-2. *J. Exp. Med.* **201**, 647–657 (2005).
41. Zhang, S. et al. Efferocytosis fuels requirements of fatty acid oxidation and the electron transport chain to polarize macrophages for tissue repair. *Cell Metab.* **29**, 443–456 (2019).
42. Hannedouche, S. et al. Oxysterols direct immune cell migration via EBI2. *Nature* **475**, 524–527 (2011).
43. Preuss, I. et al. Transcriptional regulation and functional characterization of the oxysterol/EBI2 system in primary human macrophages. *Biochem. Biophys. Res. Commun.* **446**, 663–668 (2014).
44. Rutkowska, A. et al. The EBI2 signalling pathway plays a role in cellular crosstalk between astrocytes and macrophages. *Sci. Rep.* **6**, 25520 (2016).
45. Harms, R. Z., Creer, A. J., Lorenzo-Arteaga, K. M., Ostlund, K. R. & Sarvetnick, N. E. Interleukin (IL)-18 binding protein deficiency disrupts natural killer cell maturation and diminishes circulating IL-18. *Front. Immunol.* **8**, 1020 (2017).

46. Zhou, T. et al. IL-18BP is a secreted immune checkpoint and barrier to IL-18 immunotherapy. *Nature* **583**, 609–614 (2020).
47. Chaix, J. et al. Cutting edge: priming of NK cells by IL-18. *J. Immunol.* **181**, 1627–1631 (2008).
48. Nielsen, C. M., Wolf, A.-S., Goodier, M. R. & Riley, E. M. Synergy between common γ chain family cytokines and IL-18 potentiates innate and adaptive pathways of NK cell activation. *Front. Immunol.* **7**, 101 (2016).
49. Rautela, J. & Huntington, N. D. IL-15 signaling in NK cell cancer immunotherapy. *Curr. Opin. Immunol.* **44**, 1–6 (2017).
50. Ferrari de Andrade, L. et al. Antibody-mediated inhibition of MICA and MICB shedding promotes NK cell-driven tumor immunity. *Science* **359**, 1537–1542 (2018).
51. Izawa, S. et al. H_2O_2 production within tumor microenvironment inversely correlated with infiltration of CD56(dim) NK cells in gastric and esophageal cancer: possible mechanisms of NK cell dysfunction. *Cancer Immunol. Immunother.* **60**, 1801–1810 (2011).
52. Jin, S. et al. NK cell phenotypic modulation in lung cancer environment. *PLoS ONE* **9**, e109976 (2014).
53. Sconocchia, G. et al. NK cells and T cells cooperate during the clinical course of colorectal cancer. *Oncoimmunology* **3**, e952197 (2014).
54. Stankovic, B. et al. Immune cell composition in human non-small cell lung cancer. *Front. Immunol.* **9**, 3101 (2018).
55. Bonacina, F. et al. Myeloid apolipoprotein E controls dendritic cell antigen presentation and T cell activation. *Nat. Commun.* **9**, 3083 (2018).
56. Gouna, G. et al. TREM2-dependent lipid droplet biogenesis in phagocytes is required for remyelination. *J. Exp. Med.* **218**, e20210227 (2021).
57. van Eijk, M. & Aerts, J. M. F. G. The unique phenotype of lipid-laden macrophages. *Int. J. Mol. Sci.* **22**, 4039 (2021).
58. Di Conza, G. et al. Tumor-induced reshuffling of lipid composition on the endoplasmic reticulum membrane sustains macrophage survival and pro-tumorigenic activity. *Nat. Immunol.* **22**, 1403–1415 (2021).
59. Nugent, A. A. et al. TREM2 regulates microglial cholesterol metabolism upon chronic phagocytic challenge. *Neuron* **105**, 837–854 (2020).
60. Jordan, J. A. et al. Role of IL-18 in acute lung inflammation. *J. Immunol.* **167**, 7060–7068 (2001).
61. Pechkovsky, D. V., Goldmann, T., Vollmer, E., Müller-Quernheim, J. & Zissel, G. Interleukin-18 expression by alveolar epithelial cells type II in tuberculosis and sarcoidosis. *FEMS Immunol. Med. Microbiol.* **46**, 30–38 (2006).
62. Barry, K. C. et al. A natural killer–dendritic cell axis defines checkpoint therapy–responsive tumor microenvironments. *Nat. Med.* **24**, 1178–1191 (2018).
63. Böttcher, J. P. et al. NK cells stimulate recruitment of cDC1 into the tumor microenvironment promoting cancer immune control. *Cell* **172**, 1022–1037 (2018).
64. Mattiuz, R. et al. Type 1 conventional dendritic cells and interferons are required for spontaneous $CD4^+$ and $CD8^+$ T-cell protective responses to breast cancer. *Clin. Transl. Immunol.* **10**, e1305 (2021).

[1]Marc and Jennifer Lipschultz Precision Immunology Institute, Icahn School of Medicine at Mount Sinai, New York, NY, USA. [2]The Tisch Cancer Institute, Icahn School of Medicine at Mount Sinai, New York, NY, USA. [3]Department of Oncological Sciences, Icahn School of Medicine at Mount Sinai, New York, NY, USA. [4]Center for Thoracic Oncology, Icahn School of Medicine at Mount Sinai, New York, NY, USA. [5]Department of Pathology and Immunology, Washington University School of Medicine, St. Louis, MO, USA. [6]Division of Hematology/Oncology, Icahn School of Medicine at Mount Sinai, New York, NY, USA. [7]Human Immune Monitoring Center, Icahn School of Medicine at Mount Sinai, New York, NY, USA. [8]Department of Genetics and Genomic Sciences, Icahn School of Medicine at Mount Sinai, New York, NY, USA. [9]Present address: Department of Pathology, Brigham and Women's Hospital, Boston, MA, USA. [10]Present address: CeMM Research Center for Molecular Medicine of the Austrian Academy of Sciences, Vienna, Austria. [11]Present address: CHU Nantes, Laboratoire d'Immunologie, Center for ImmunoMonitoring Nantes-Atlantique (CIMNA), Nantes, France. [12]Present address: Cancer Immunity Laboratory, Molecular Oncology Program, Spanish National Cancer Center (CNIO), Madrid, Spain. [13]These authors contributed equally: Matthew D. Park, Ivan Reyes-Torres. ✉e-mail: miriam.merad@mssm.edu

Methods

Materials availability

The study did not generate new unique reagents.

Mouse strains and tumor cell lines

C57BL/6J-*Trem2*^{em2Adiuj}/J (*Trem2*$^{-/-}$) and B6.129P2-*Il18r1*^{tm1Aki}/J (*Il18r1*$^{-/-}$) mice were purchased from The Jackson Laboratory. Both these and WT C57BL/6 mice used as controls for experimentation were either bred at the Icahn School of Medicine at Mount Sinai or purchased from The Jackson Laboratory and housed for a minimum of 7 d before experimental use. For bone-marrow transplantation, B6.SJL-*Ptprc*^{a}*Pepc*^{b}/BoyJ (CD45.1) mice were also purchased from The Jackson Laboratory.

Mice were maintained at specific-pathogen-free health status in individually ventilated cages at 21–22 °C and 39–50% humidity. All animal procedures were approved by the Institutional Animal Care and Use Committee (IACUC) of the Icahn School of Medicine at Mount Sinai. Mice within experiments were age and sex matched. All studies performed on mice were conducted in accordance with the IACUC at the Icahn School of Medicine at Mount Sinai.

Murine tumor models

To model primary lung adenocarcinoma, mice were intravenously injected via the tail vein with *Kras*$^{G12D/+}$*p53*$^{-/-}$ (KP) lung epithelial cells, KP cells engineered to express GFP (KP-GFP) or KP cells expressing both GFP and OVA (KP-GFP-OVA) (5×10^5 cells per mouse in 250 µl phosphate-buffered saline (PBS)). KP cells were grown in complete cell culture medium (RPMI + 10% FBS + 1% P/S) and were detached for use at 70% confluence using 0.25% trypsin. The tumor cells were originally derived from KP mice[25] generated by crossing LSL-*Kras*$^{G12D/+}$ mice (The Jackson Laboratory) with *p53*$^{fl/fl}$ mice (The Jackson Laboratory). Tumor-bearing lungs were analyzed at 22 or 28 d after injection of KP or KP-GFP tumors and at 7–8 weeks after injection of KP-GFP-OVA tumors, except when otherwise indicated. For anti-MICA experiments, the C57BL/6-derived metastatic melanoma cell line B16-F10 expressing human MIC-A was provided by L. Ferrari De Andrade (Icahn School of Medicine at Mount Sinai) and intravenously injected at 2.5×10^5 cells per mouse. Mice were analyzed at 21 d after injection and tumor quantification was performed on H&E-stained slides of formalin-fixed paraffin-embedded 4-µm lung tissue sections. Slides were scanned using an Olympus digital scanner and analyzed using the Panoramic viewer and QuPath software.

Antibody-mediated blockade and depletion studies

To deplete CD8$^+$ T cells and NK cells, mice were intraperitoneally injected with anti-CD8α (BioXCell, clone 2.43) and anti-NK1.1 (BioXCell, clone PK136), respectively. Blocking antibodies used for experimentation include anti-IL-18 (BioXCell, clone YIGIF74-1G7), anti-IL-15 (BioXCell, clone AIO.3) and the corresponding isotype antibodies for both. The TREM2 antibody and its isotype control, both of which were provided by M. Colonna (Washington University School of Medicine at St. Louis), were used to assess therapeutic blockade of TREM2. For each treatment regimen, mice received an initial dose at 200 µg per mouse at 14 d after injection of tumor cells, followed by subsequent 100 µg every other day. The MIC-A stabilizing antibody, provided by F. De Andrade (Icahn School of Medicine at Mount Sinai), was given as single doses of 200 µg per mouse on days 6, 9, 13, 15 and 19 after tumor challenge.

Bone-marrow reconstitution

Donor bone-marrow cells were isolated from femur exudates of WT and *Trem2*$^{-/-}$ mice bred at the Icahn School of Medicine at Mount Sinai. Transplantation was performed by retro-orbitally injecting 5×10^5 donor cells into sublethally irradiated (twice, 6.5 Gy, 6 h apart). Recipients were supplemented with sulfamethoxazole/trimethoprim for 3 weeks. Successful reconstitution was assessed by flow cytometric analysis of peripheral blood.

Flow cytometry and fluorescence-activated cell sorting

Single-cell suspensions from perfused murine lungs were obtained upon lung tissue digestion with collagenase IV (0.25 mg ml^{-1}; Sigma) at 37 °C for 30 min in agitation (90 r.p.m.) followed by passing through a 70-µm cell strainer and red blood cell lysis (RBC lysis buffer, BioLegend) for 5 min at room temperature. For flow cytometry or FACS, cells were stained in FACS buffer (PBS supplemented with 2% bovine serum albumin (BSA) and 5 mM EDTA) with different combination of the following monoclonal antibodies (1:200 dilution) specific to: CD45 (clone 30-F11, BioLegend; cat. no. 103137); CD45.1 (clone A20, BioLegend); CD45.2 (clone 104, BioLegend); B220 (clone RA3-6B, BioLegend); CD19 (clone eBio1D3, eBiosciences); Ly6G (clone 1A8, BioLegend; cat. no. 127621); CD64 (clone X54-5/7.1, BioLegend); MerTK (clone 2B10C42, BioLegend); CD2 (clone RM2-5, BioLegend; cat. no. 100113); Siglec-F (clone E50-2440, BD Pharmingen; cat. no. 740956); MHC-I-A/I-E (clone M5/114.15.2, eBiosciences; cat. no. 12-5321-82); CD11b (clone M1/70, eBiosciences; cat. no. 45-0112-82); CD11c (clone N418, Invitrogen; cat. no. 47-0114-82); CD24 (clone M1/69; Invitrogen; cat. no. 25-0242-82); CD103 (clone 2E7, BioLegend; cat. no. 17-1031-82); XCR1 (clone ZET, BioLegend); CD107a (clone 1D4B, BioLegend); CD3 (clone 145-2C11, eBiosciences); CD8a (clone 53-6.7, BioLegend; cat. no. 558106); CD4 (clone GK1.5, eBiosciences; cat. no. 17-0041-82); CD44 (clone IM7, BioLegend); PD-1 (clone RMP1-30, BioLegend); TCF-1 (clone 7F11A10, BioLegend), Granzyme-B (clone GB11, Thermo Fisher); NK1.1 (clone PK136, BioLegend); NKp46 (clone 29A1.4, BioLegend); CD49b (clone DX5, Thermo Fisher); CD49a (clone HMa1, BioLegend); KLRG1 (clone MAFA, BioLegend); NKG2D (clone C7, BioLegend); TNF (clone MP6-XT22, eBiosciences; cat. no. 17-7321-82); and IFN-γ (clone XMG1.2, eBiosciences; cat. no. 25-7311-41). For intracellular staining, cells were fixed with either BD Cytofix/Cytoperm kit for cytokine stains or with the eBiosciences Foxp3 transcription factor kit for intranuclear stains, both according to the manufacturer's instructions. For T cell cytokine stains, cells were incubated with 10 µg ml^{-1} brefeldin A, 0.2 µg ml^{-1} ionomycin and 0.5 µg ml^{-1} phorbol myristate acetate (Sigma) for 3 hat 37 °C followed by staining of surface markers and fixation. For flow cytometry, cells were analyzed in a BD LSR Fortessa analyzer (BD Biosciences). For FACS, cells were prepared, stained and purified using a BD FACSAria sorter (BD Biosciences). Flow cytometry data were acquired using FACS Diva software v.7 (BD) and the data obtained were analyzed using FlowJo (LLC).

In vitro culture of bone-marrow-derived macrophages

Bone-marrow cells were isolated by flushing murine femurs, tibias and humeri with PBS (0.5% BSA and 2 nM EDTA, 1% P/S). Cells were strained through a 70-µm filter and centrifuged before resuspension in 1× RBC lysis buffer (BioLegend) for 5 min at room temperature.

Total bone-marrow cells were plated in non-tissue-culture-treated dishes with RPMI medium, supplemented with 10% fetal calf serum, 1% P/S and 200 ng ml^{-1} of murine recombinant colony stimulating factor 1 (CSF1) (Peprotech) (differentiation medium). After 4 d of differentiation, non-adherent cells were aspirated and washed with PBS to enrich for highly adherent cells. Fresh medium was added and supplemented with 200 ng ml^{-1} of recombinant murine GM-CSF (Peprotech). Monocyte-derived cells were then cultured with GM-CSF for 24 h, then medium was refreshed before supplementation with 200 ng ml^{-1} of recombinant murine IL-4 (Shenandoah Biotechnology) for 24 h. This was then substituted for differentiation medium. On day 7, apoptotic KP-GFP cells (generated by exposure to UV irradiation for 12 h) were added to mo-mac cultures for 4 h. Some macrophages were left unexposed as controls. Cells were then detached using cold PBS supplemented with EDTA and gentle pipetting. Mo-macs were FACS-sorted into 500 µl of Trizol for downstream analysis.

To assess the effect of TREM2 deficiency on the ability for mo-macs to directly influence the activation and proliferation of NK cells, splenocytes from either WT or *Il18r1*$^{-/-}$ mice were enriched for NK cells via

negative selection (Miltenyi Biotec) and splenic NK cells were added to cultures of fed mo-macs generated from either WT or *Trem2*$^{-/-}$ mice in a 1:10 ratio. The cell mixture was stimulated with recombinant IL-18 (1 nM) (R&D Systems, cat. no. 9139-IL) and IL-12 (10 ng ml^{-1}) (R&D Systems, cat. no. 419-ML) with brefeldin A (5 mg ml^{-1}, 1:250 dilution). After 4 h, NK cells were collected for flow cytometry.

Ultra-low-input bulk RNA-sequencing

For ultra-low-input bulk RNA-sequencing, 10^4–10^5 GFP^{hi} and GFP^{lo} mo-macs were sorted from digested KP-GFP tumor-bearing lungs by FACS into 500 µl TRIzol. RNA was then extracted using an RNeasy Micro kit (QIAGEN), according to the manufacturer's instructions. RNA was quantified and quality controlled using a Qubit and a Bioanalyzer. Between 0.5–1 ng RNA was retrotranscribed and processed to complementary DNA libraries using the Smart-Seq v.4 Ultra-Low-Input RNA kit for sequencing (Takara Bio). Libraries were sequenced on an Illumina NextSeq 550 system.

Differential gene expression testing

Raw bulk RNA-seq data was processed and aligned to genome reference mm10 using the R package Rsubread with default parameters. Gene expression normalization and differential expression analyses were conducted using *DESeq2*, with genotype, antigen condition and replicate as design matrix input. To account for batch effects across replicates, limma batch-effect correction was applied on the normalized counts before gene expression heat map visualizations. Differentially expressed genes were called using $\log_2$(fold change) > 1 and adjusted $P < 0.1$. Volcano plots were generated using R packages ggplot and seriation.

Sample preparation for scRNA-seq

Single-cell suspensions from lung tissues were obtained, as described above. For scRNA-seq, these cells were suspended and stained in 100 µl multiplex hashing antibodies at 4 °C for 20 min. Stained cells were washed three times in PBS + 0.5% BSA to remove unbound antibodies. Washed cells were resuspended in 150 µl wash buffer and counted using a Nexcelom Cellometer Auto2000. Hashed samples were pooled in equal amounts of live cells. Volume was adjusted to achieve a target of 2×10^6 cells ml^{-1}. Hashed samples were loaded onto 10x Genomics NextGen 5′ v.1.1 assay, as per the manufacturer's instructions, for a target cell recovery of 20,000 cells per lane. Libraries were constructed, as per the manufacturer's instructions. During cDNA amplification, hashtag oligonucleotides (HTOs) were enriched during cDNA amplification with the addition of 3 pmol HTO Additive primer (5′GTGACTGGAGTTCAGACGTGTGCTC). This PCR product was isolated from the mRNA-derived cDNA via SPRISelect size selection and libraries were made as per the New York Genome Center Hashing protocol. All libraries were quantified via Agilent 2100 hsDNA Bioanalyzer and KAPA library quantification kit (Roche, cat. no. 0796014001.) Gene expression libraries were sequenced at a targeted depth of 25,000 reads per cells and HTO libraries were sequenced at a targeted read depth of 1,000 reads per cell. All libraries were sequenced on the Illumina NovaSeq S2 100 cycle kit with run parameters set to 28 × 8 × 0 × 60 (R1 × i7 × i5 × R2).

scRNA-seq analysis

After library demultiplexing, gene expression libraries were aligned to the mm10 reference transcriptome and count matrices were generated using the default CellRanger 2.1 workflow, using the 'raw' matrix output. Where applicable, doublets were removed based on co-staining of distinct sample-barcoding ('Hashing') antibodies (maximum staining antibody counts/second-most staining antibody counts <5). Following alignment, cell barcodes corresponding to cells that contained >500 UMIs were extracted. From among these, cells whose transcripts constituted >25% mitochondrial genes were filtered from downstream analyses. The R package Seurat was used to scale the data, transform via a log normalization method, adjust for batch correction, cluster cells based on shared nearest neighbors and perform dimensionality reduction based on the first 15 principal components. Gene module analyses was performed, based on the identification of groups of highly correlated genes, according to the Pearson correlation matrix of the most variable genes. This was performed using the R package scDissector. Highly correlated gene were assigned into groups by hierarchical clustering. Differentially expressed genes were identified using the FindMarkers function in Seurat. Average UMI expression values were imputed to determine log fold change differences between cell types to further the analysis of markers of interest. Gene set enrichment analysis for the identification of active signaling pathways was performed by querying genes of interest through the Enrichr database[55,62,63]. Other R packages used for data analysis include: scDissector v.1.0.0; shiny v.1.7.1; shinyTree v.0.2.7; heatmaply v.1.3.0; plotly v.4.10.0; ggvis v.0.4.7; ggplot2 v.3.3.5; dplyr v.1.0.7; Matrix v.0.9.8; and seriation v.1.3.5.

scRNA-seq of human NSCLC lesions and non-involved lung tissues

A scRNA-seq dataset of immune cells isolated from resected NSCLC lesions and matched, non-involved adjacent lung tissues from 35 patients was used to probe the relative distribution of NK cells and mo-macs and to identify a conserved molecular program across mo-mac subsets[65]. Human samples for this particular study were collected by the Cancer BioRepository at the Icahn School of Medicine at Mount Sinai.

Multiplex imaging of human and murine tissue sections

Formalin-fixed paraffin-embedded tissue sections (4 µm) were stained using the Multiplexed Immunohistochemical Consecutive Staining on a Single Slide protocol, as previously described[66]. Briefly, slides were baked at 50 °C overnight, deparaffinized in xylene and rehydrated in decreasing concentration of ethanol (100%, 90%, 70%, 50% and dH_2O). Sample slides were incubated in pH 6 or pH 9 buffers at 95 °C for 30 min for antigen retrieval, then in 3% hydrogen peroxide for 15 min and in serum-free protein block solution (Dako) for 30 min. Primary antibody staining was performed using the optimized dilution during 1 h at room temperature or at 4 °C overnight followed by signal amplification using associated secondary antibody conjugated to horseradish peroxidase during 30 min. Chromogenic revelation was performed using AEC (Vector). Tissue sections were counterstained with hematoxylin, mounted with a glycerol-based mounting medium and finally scanned to obtain digital images (Aperio AT2, Leica). Then, the same slides were bleached and stained again as previously described[66]. Primary antibodies were anti-human CD68 (clone KP1, Dako) and anti-human TREM2 (D8I4C, Cell Signaling Technology) and anti-mouse NKp46 (AF2225, BioLegend). Quantification of positively stained cells were performed using the positive cell detection algorithm in the QuPath software with default settings.

Immunofluorescence imaging of murine tissue sections

Perfused lungs isolated from tumor-bearing mice were fixed overnight at 4 °C in paraformaldehyde, cryopreserved using the sucrose gradient method (2 h of successive incubations in 10, 20 and 30% sucrose in PBS), then embedded and frozen in Optimal Cutting Temperature compound Tissue-Plus (Thermo Fisher). Frozen tissue sections were thawed and permeabilized with 0.1% Triton-X-100 for 10 min. Blocking was performed using 10% BSA + 2% normal goat serum in PBS for 1 h. Sections were incubated with primary antibodies for 3 d at 4 °C, then with secondary antibodies for 1 h at room temperature. Mounting was conducted using ProLong Gold Antifade Reagent with DAPI (Invitrogen, P36931), anti-TREM2 (clone AF1729, R&D Systems, 1:100 dilution) and anti-GFP (clone ab13970, Abcam, 1:200 dilution) were used as primary or directly conjugated antibodies, respectively.

Alexa Fluor donkey anti-sheep 555 (Abcam, ab150178) was used as secondary antibody for TREM2 staining. Imaging was performed using a Zeiss 780 Confocal Microscope. Quantification of fluorescence intensity and post-acquisition processing of images was performed using ImageJ software and ZEN Black Imaging Software (Zeiss). For imaging of FACS-sorted mo-macs, between 10^3–10^4 GFP^{hi} and GFP^{lo} mo-macs were FACS-sorted and centrifuged into Alcian-blue-treated coverslips and fixed in 1% paraformaldehyde. Cells were permeabilized in 0.1% Triton-X in PBS for 10 min at room temperature. Coverslips were washed with PBS and stained with an anti-GFP antibody for 2 h at room temperature. Next Coverslips were washed with PBS again (2×) and stained with DAPI (1 ng ml^{-1}) for 5 min. Finally, coverslips were mounted using Prolong Gold Antifade and sections were imaged on a Zeiss 780 Confocal Microscope.

Quantitative PCR

RNA was retrotranscribed to cDNA using the RNA to cDNA EcoDry Premix (Double Primed) kit (Takara). Transcripts were quantified using the system AB7900-FAST-384 with a two-step reverse-transcription qPCR process. KiCqStart SYBR Green Primers pre-designed and customized were purchased from Sigma-Aldrich. Quantitative PCR using primers for CD45 mRNA was conducted in each plate to provide a normalization reference. Quantification of relative gene expression was calculated by the comparative Ct method ($2 - \Delta\Delta Ct$), relative to CD45 Ct. Primer sequences are provided below (5′ to 3′):

Apoe → F:CTGACAGGATGCCTAGCCG, R:CGCAGGTAATCCCAGAAGC;

Gpnmb → F:CATTCCCATCTCGAAGGTGAAA, R:AAATGGCAGAGTCGTTGAGGA;

Trem2 → F:CTGGAACCGTCACCATCACTC, R:CGAAACTCGATGACTCCTCGG.

Statistics and reproducibility

From scRNA-seq data, we excluded cells based on pre-established criteria for single-cell exclusion, such as low number of detected transcripts (based on UMI counts) and high mitochondrial or RBC-associated transcriptome content. Cell filtering for the human data is noted by Leader et al.[13]. Outlier detection was based on the extreme Studentized deviate method and samples identified as such were removed from further analysis.

Reporting summary

Further information on research design is available in the Nature Portfolio Reporting Summary linked to this article.

Data availability

All murine sequencing data will be made publicly available (GSE184304, GSE184309 and GSE184317). The human dataset is available at the Sequence Read Archive with BioProject accession no. PRJNA609924. Source data are provided with this paper.

Code availability

All murine sequencing code will be made publicly available (GSE184304, GSE184309 and GSE184317). No custom code was generated for this study. Code for generating figures can be provided upon reasonable request.

References

65. Bonnardel, J. et al. Stellate cells, hepatocytes, and endothelial cells imprint the Kupffer cell identity on monocytes colonizing the liver macrophage niche. *Immunity* **51**, 638–654 (2019).
66. Browaeys, R., Saelens, W. & Saeys, Y. NicheNet: modeling intercellular communication by linking ligands to target genes. *Nat. Methods* **17**, 159–162 (2019).

Acknowledgements

We thank members of the Merad and Brown laboratories at the Marc and Jennifer Lipschultz Precision Immunology Institute at Mount Sinai and the Tisch Cancer Institute for insightful discussions and feedback; we specifically thank M.J. Lin and J. Brody for lending us flow cytometry antibodies against the NKG2D ligands; the Mount Sinai Flow Cytometry Core, the Human Immune Monitoring Center and the Mount Sinai Biorepository for support. Data in this paper were used in a dissertation as partial fulfillment of the requirements for a PhD at the Graduate School of Biomedical Sciences at Mount Sinai.

Author contributions

M.M. conceived the project. M.M., M.D.P. and I.R.T. wrote the manuscript. I.R.T., M.D.P. and M.M. designed the experiments. I.R.T., M.D.P., J.L.B., N.M.L., E.H., S.H., M.B., A.N. and A.R.S. performed experiments. I.R.T., M.D.P., J.L.B. and A.N. maintained mouse colonies and cell cultures for these experiments. M.D.P. and A.M. performed computational analyses, with additional support from T.D., D.D. and S.H. P.H., L.T. and J.G. provided immunohistochemistry stains and analyses. M.M., J.H. and M.C. provided the TREM2 blocking antibody and isotype control. J.N., A.F. and N.B. provided the IL-15 neutralizing antibody; M.J.L. and J.B. provided the antibodies against NKG2D ligands; and L.F.A. provided the MIC-A stabilizing antibody and B16-F10-MICA cell line. A.R.S., B.M., J.C.M., E.K., A.O.K., M.C.A., N.B., A.H., L.F.A., B.D.B., M.C. and T.U.M. provided intellectual input. This work was supported by National Institutes of Health grants R01 AI153363 (to A.O.K.), R01 CA254104 and R01 CA257195 (to M.M. and B.D.B.), 1R37 CA269982-01A1 (to L.F.d.A.), R01CA262684 to M.C. S.H. was supported by the National Cancer Institute predoctoral-to-postdoctoral fellowship K00 CA223043. N.M.L. was supported by the Cancer Research Institute/Bristol Myers Squibb Irvington Postdoctoral Research Fellowship to Promote Racial Diversity (award no. CRI3931). B.D.B. and M.M. were supported by the Applebaum Foundation and the Feldman Foundation. B.D.B. was supported by the Alliance for Cancer Gene Therapy. L.F.d.A. is the recipient of a Cancer Research Institute Clinic and Laboratory Integration Program Grant (award no. CRI3483), Tisch Cancer Institute Developments Funds Award (P30CA196521), Department of Defense Career Development Award (W81XWH2210262 and project number CA210940), Leukemia and Lymphoma Society (award no. 6647-23) and is supported by the Elsa U. Pardee Foundation.

Competing interests

L.F.d.A. is a named inventor of the MIC-A therapeutic antibody in a filed patient (US20200165343A1) and has received royalty payments in relation to this therapeutic. L.F.d.A. is also co-inventor in issued patents about an α-3 domain-specific antibody. M.C. receives research support from NGM Biotechnology and Vigil Neuro, is a scientific advisory board member of NGM Biotechnology and Vigil Neuro and has a patent for TREM2 pending. M.M. serves on the scientific advisory board and holds stock from Compugen, Myeloid Therapeutics, Morphic Therapeutic, Asher Bio, Dren Bio, Nirogy, Oncoresponse, Owkin, Pionyr, OSE and Larkspur. M.M. serves on the scientific advisory board Innate Pharma, DBV and Genenta. M.M. is a named co-inventor on an issued patent for multiplex immunohistochemistry to characterize tumors and treatment responses. The technology is filed through Icahn School of Medicine at Mount Sinai and is currently unlicensed. This technology was used to evaluate tissue in this study and the results could impact the value of this technology. The remaining authors declare no competing interests.

Additional information

Extended data is available for this paper at https://doi.org/10.1038/s41590-023-01475-4.

Supplementary information The online version contains supplementary material available at https://doi.org/10.1038/s41590-023-01475-4.

Correspondence and requests for materials should be addressed to Miriam Merad.

Peer review information *Nature Immunology* thanks Florian Greten and the other, anonymous, reviewer(s) for their contribution to the peer review of this work. Primary Handling Editor: S. Houston in collaboration with the *Nature Immunology* team.

https://doi.org/10.1038/s41590-023-01475-4

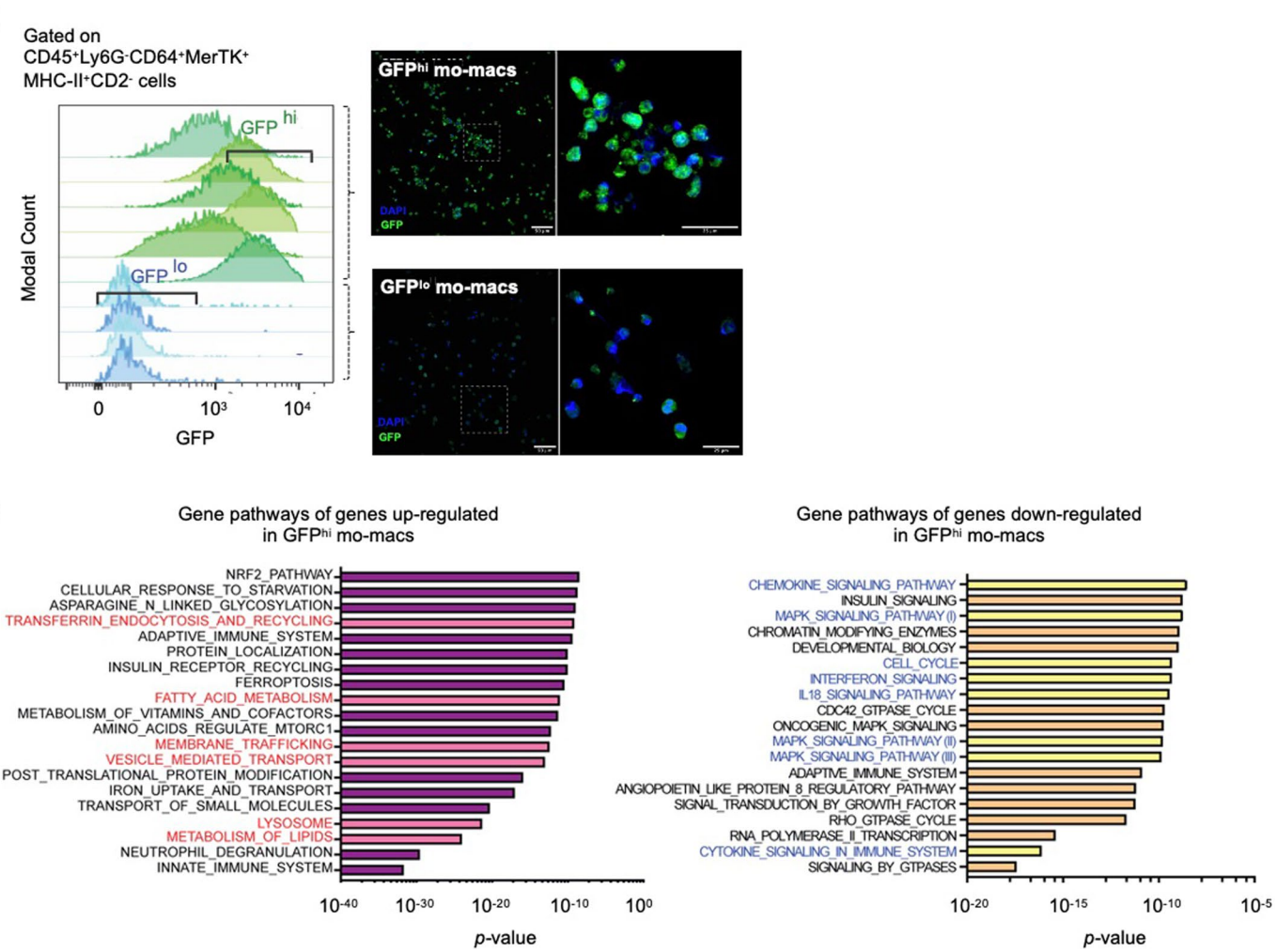

Extended Data Fig. 1 | Purification and active signaling pathways in GFP^{lo} and GFP^{hi} mo-macs. (**a**) Flow cytometry sort strategy (left) for purifying GFP^{hi} and GFP^{lo} mo-macs from single-cell suspensions of digested KP-GFP tumor-bearing lungs at four weeks post-inoculation of KP-GFP cells. Histograms show the fluorescence spectrum of GFP in mo-macs from tumor-bearing lungs, comprised of GFP^{hi} (green) and GFP^{lo} (blue) mo-macs. Each row represents an individual replicate. Representative confocal immunofluorescence (IF) imaging of FACS-sorted GFP^{lo} and GFP^{hi} mo-macs (right). For each pair of images, a broad-field view with a region of interest (ROI, white outline) (left) and a magnification of the ROI (right) are shown. Data is representative of two independent experiments. (**b**) Gene set enrichment analysis (GSEA) (Broad Institute) for pathways annotated in the KEGG and Reactome databases performed on the significantly differentially regulated genes in GFP^{hi} mo-macs, relative to GFP^{lo} mo-macs. The top 15 most significantly enriched terms are shown, with notable pathways highlighted in red for up-regulated genes in GFP^{hi} mo-macs (left) and up-regulated genes in GFP^{lo} mo-macs (right).

https://doi.org/10.1038/s41590-023-01475-4

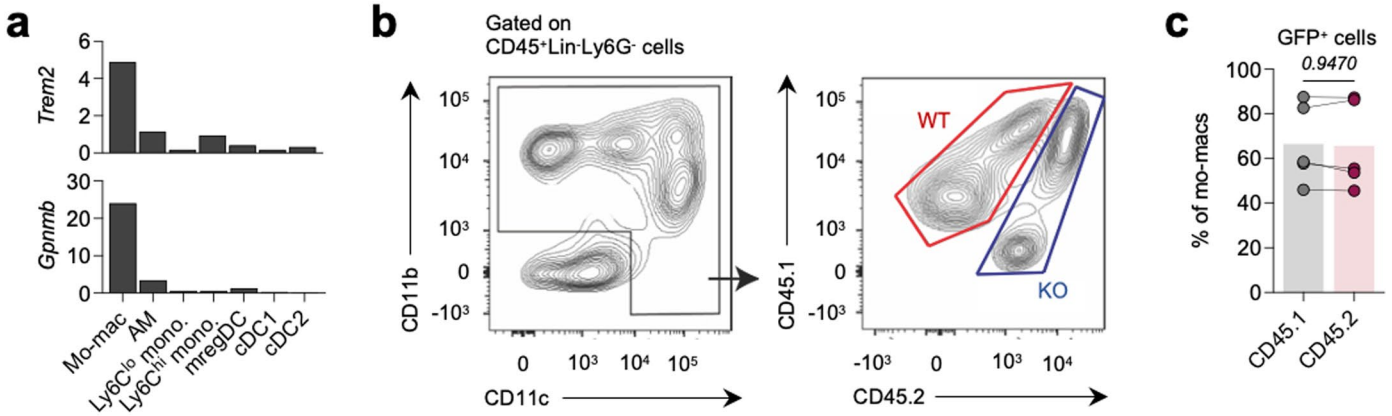

Extended Data Fig. 2 | scRNA-seq profiling of mo-macs in chimeric mice. (**a**) Expression of *Trem2* and *Gpnmb*, as hallmark genes of the TREM2 gene program, across cell subtypes (mo-macs, AMs, Ly6C^{lo} and Ly6C^{hi} monocytes, mregDCs, cDC1 and cDC2) identified by unsupervised clustering. (**b**) Flow cytometry sort strategy to purify CD45.1 WT and CD45.2 KO fractions of MNPs from KP-GFP tumor-bearing chimeric mice. (**c**) Flow cytometric quantification of GFP^{+} mo-macs, represented as relative frequency among total mo-macs from the purified CD45.1 WT and CD45.2 KO fractions of MNPs from KP-GFP tumor-bearing mice. Paired values shown for paired CD45.1 WT and CD45.2 KO cells that were purified from the same biological replicate. (mean ± standard error of mean (S.E.M.); paired two-tailed *t*-test at a 95% confidence interval).

https://doi.org/10.1038/s41590-023-01475-4

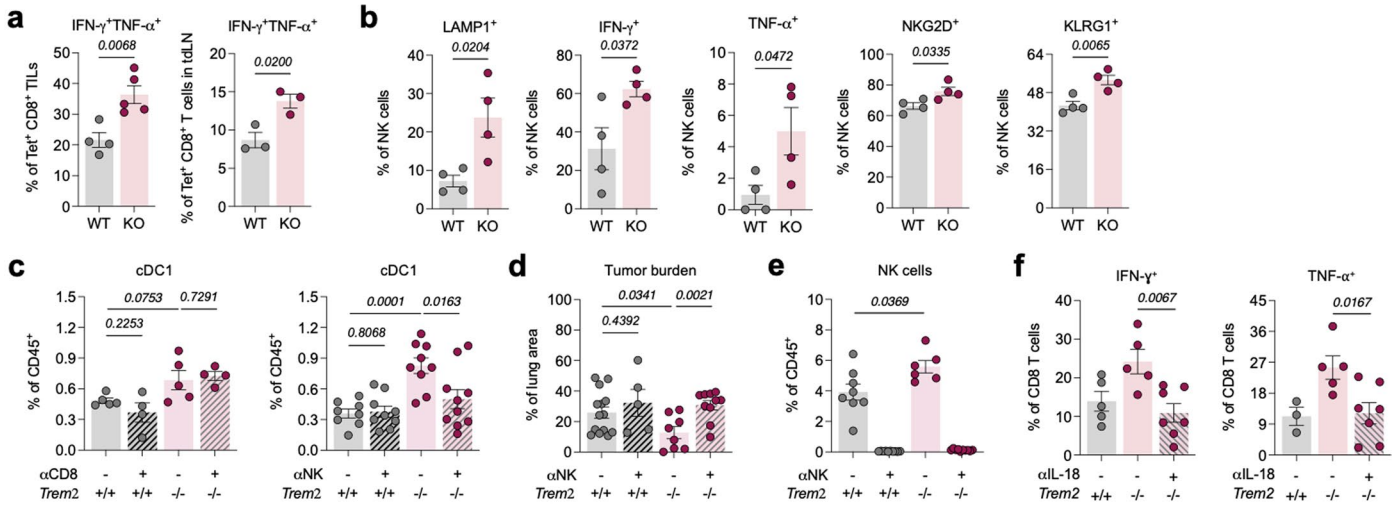

Extended Data Fig. 3 | Contributions of CD8 T cells and NK cells to tumor regression in KO mice. (**a**) Flow cytometric quantification of IFN-γ/TNF-α-producing CD8 T cells, as a relative frequency of total antigen-specific CD8 T cells, in the tumor-bearing lungs (left) and in the tumor-draining lymph nodes (tdLN) (right) of KP-GFP tumor-bearing WT and KO mice. (n = 4-5 mice per group, mean ± standard error of mean (S.E.M.); unpaired two-tailed *t*-test at a 95% confidence interval). (**b**) Flow cytometric quantification of NK cells expressing activation/degranulation markers, as a relative frequency of total NK cells. (n = 4-5 mice per group, mean ± standard error of mean (S.E.M.); unpaired two-tailed *t*-test at a 95% confidence interval). (**c**) Flow cytometric quantification of type 1 conventional dendritic cells (cDC1), as a relative frequency of $CD45^+$ immune cells, in the tumor-bearing lungs of WT mice and KO mice treated with either an isotype control or CD8 (right) (n = 4-5 mice per group) or NK cell (left)-depleting antibody (n = 8-10 mice per group). (mean ± standard error of mean (S.E.M.); unpaired two-tailed *t*-test at a 95% confidence interval. Data is representative of two independent experiments.). (**d**) Quantification of the tumor area as a percent of the total area of the lung cross-section from tumor-bearing lungs of WT and KO mice treated with either an isotype control of NK cell-depleting antibody. (n = 8-10 mice per group, mean ± standard error of mean (S.E.M.); unpaired two-tailed *t*-test at a 95% confidence interval. Data shown is of at least two independent experiments.). (**e**) Flow cytometric quantification of NK cells, as a relative frequency of $CD45^+$ immune cells. (n = 8-10 mice per group, mean ± standard error of mean (S.E.M.); unpaired two-tailed *t*-test at a 95% confidence interval. Data is representative of at least three independent experiments.). (**f**) Flow cytometric quantification of IFN-γ-producing (left) and TNF-α-producing (right) CD8 T cells in the tumor-bearing lungs of WT mice with isotype antibody, KO mice with isotype antibody, and KO mice given IL-18 neutralizing antibody. Data shown as a relative frequency among total CD8 T cells. (n = 5-8 mice per group, mean ± standard error of mean (S.E.M.); unpaired two-tailed *t*-test at a 95% confidence interval. Data shown is representative of at least three independent experiments).

https://doi.org/10.1038/s41590-023-01475-4

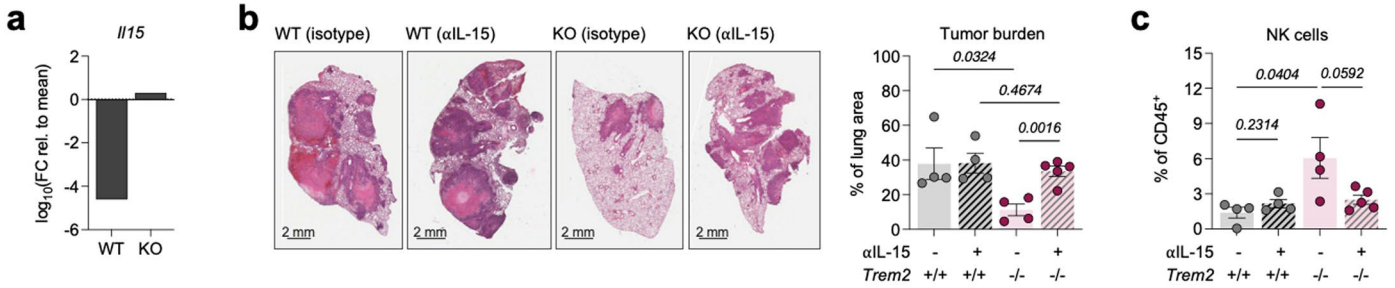

Extended Data Fig. 4 | Cooperative IL-15 signaling is needed to confer the therapeutic benefit of a TREM2-deficient setting. (**a**) Relative expression of *Il15* by mature mregDCs, as determined by scRNA-seq profiling of MNPs in the tumor-bearing lungs of WT and KO mice (Fig. 3C). (**b**) Representative H&E images of tumor-bearing lungs of WT, isotype antibody ($n = 4$), WT mice that received the IL-15 neutralizing antibody ($n = 4$), KO, isotype antibody ($n = 4$), KO mice that received the IL-15 neutralizing antibody ($n = 5$) (left). Quantification of the tumor area as a percent of the total area of the lung cross-section (right) is shown. (mean ± standard error of mean (S.E.M.); unpaired two-tailed *t*-test at a 95% confidence interval). (**c**) Flow cytometric quantification of NK cells, as a relative frequency of $CD45^+$ immune cells, in the KP-GFP tumor-bearing lungs of isotype control WT and KO mice and WT and KO mice treated with the αIL-15 antibody. (n = 4-5 mice per group, mean ± standard error of mean (S.E.M.); unpaired two-tailed *t*-test at a 95% confidence interval. Data shown is representative of two independent experiments).

nature portfolio

Corresponding author(s): Miriam Merad

Last updated by author(s): Feb 10, 2023

Reporting Summary

Nature Portfolio wishes to improve the reproducibility of the work that we publish. This form provides structure for consistency and transparency in reporting. For further information on Nature Portfolio policies, see our Editorial Policies and the Editorial Policy Checklist.

Statistics

For all statistical analyses, confirm that the following items are present in the figure legend, table legend, main text, or Methods section.

n/a	Confirmed	
☐	☒	The exact sample size (*n*) for each experimental group/condition, given as a discrete number and unit of measurement
☐	☒	A statement on whether measurements were taken from distinct samples or whether the same sample was measured repeatedly
☐	☒	The statistical test(s) used AND whether they are one- or two-sided *Only common tests should be described solely by name; describe more complex techniques in the Methods section.*
☒	☐	A description of all covariates tested
☐	☒	A description of any assumptions or corrections, such as tests of normality and adjustment for multiple comparisons
☐	☒	A full description of the statistical parameters including central tendency (e.g. means) or other basic estimates (e.g. regression coefficient) AND variation (e.g. standard deviation) or associated estimates of uncertainty (e.g. confidence intervals)
☐	☒	For null hypothesis testing, the test statistic (e.g. *F*, *t*, *r*) with confidence intervals, effect sizes, degrees of freedom and *P* value noted *Give P values as exact values whenever suitable.*
☒	☐	For Bayesian analysis, information on the choice of priors and Markov chain Monte Carlo settings
☒	☐	For hierarchical and complex designs, identification of the appropriate level for tests and full reporting of outcomes
☐	☒	Estimates of effect sizes (e.g. Cohen's *d*, Pearson's *r*), indicating how they were calculated

Our web collection on statistics for biologists contains articles on many of the points above.

Software and code

Policy information about availability of computer code

Data collection	Flow sorting data was collected using BD FACSDiva software v.7 on a BD LSRFortessa analyzer and BD FACSAria II. Confocal microscopy was performed with a Zeiss LSM 780 system (ZEISS).

Data analysis	Flow cytometry data was analyzed using the FlowJo v10.8.1. Microscopy images were processed with the Zeiss LSM Image Browser and ImageJ software (version 1.43). Histological images were processed and analyzed using the QuPath software. For scRNAseq data, mouse assembly version mm10/NCBI m38 was used for sequence alignment using vowtie v.2.3.4.1. Data analysis of scRNAseq data was completed with the published Seurat (v.4.1.0) package. Additional R packages used in the analysis include: scDissector v.1.0.0 shiny v.1.7.1 shinyTree v.0.2.7 heatmaply v.1.3.0 plotly v.4.10.0 ggvis v.0.4.7 ggplot2 v.3.3.5 dplyr v.1.0.7 Matrix v.0.9.8 seriation v.1.3.5 Methods pertaining to clustering, cell type signature generation, projection, and other analyses were performed as previously described (see Methods). No custom code was generated for this study. Scripts are nonetheless available upon request.

For manuscripts utilizing custom algorithms or software that are central to the research but not yet described in published literature, software must be made available to editors and reviewers. We strongly encourage code deposition in a community repository (e.g. GitHub). See the Nature Portfolio guidelines for submitting code & software for further information.

Data

Policy information about availability of data

All manuscripts must include a data availability statement. This statement should provide the following information, where applicable:

- Accession codes, unique identifiers, or web links for publicly available datasets
- A description of any restrictions on data availability
- For clinical datasets or third party data, please ensure that the statement adheres to our policy

All murine sequencing data is available at the following accession codes (GSE184304, GSE184309, GSE184317). The human scRNAseq dataset referenced in this study is published and data files are available at the Sequence Read Archive (SRA) with BioProject accession PRJNA609924.

Human research participants

Policy information about studies involving human research participants and Sex and Gender in Research.

Reporting on sex and gender	No new data was generated from human research participants. Single-cell RNA-sequencing data used to generate results in Figure 1 was published by Leader et al. and can be found at the accession codes detailed above.
Population characteristics	N/A
Recruitment	N/A
Ethics oversight	N/A

Note that full information on the approval of the study protocol must also be provided in the manuscript.

Field-specific reporting

Please select the one below that is the best fit for your research. If you are not sure, read the appropriate sections before making your selection.

☒ Life sciences ☐ Behavioural & social sciences ☐ Ecological, evolutionary & environmental sciences

For a reference copy of the document with all sections, see nature.com/documents/nr-reporting-summary-flat.pdf

Life sciences study design

All studies must disclose on these points even when the disclosure is negative.

Sample size	No statistical methods were used to determine sample sizes, though preliminary experiments were leveraged to estimate appropriate sample sizes, with an effort to achieve a minimum of n=3 mice, per experimental group per experiment, which proved sufficient to ascertain reproducible and biologically-relevant results. The sample sizes reported in the present study are comparable to those used in previous and similar publications. All experiments were performed with distinct biological replicates for in vivo studies and further validated with technical replicates for in vitro experiments, including co-culture experiments, as indicated in the text and in the figure legends. For in vivo studies, in particular, variation amongst mice that were inoculated with tumor cells was taken into consideration.
Data exclusions	From the scRNAseq data, we excluded cells based on pre-established criteria for single-cell exclusion, such as low number of detected

Data exclusions	transcripts (based on UMI counts) and high mitochondrial or red blood cell-associated transcriptome content. Cell filtering for the human data is noted in Leader et al. (2021). For biological experiments, outlier detection was based on the extreme studentized deviate method, and samples identified as such were removed from further analysis.
Replication	All in vivo and in vitro experiments were performed at least twice. Experiments performed in excess of that are noted in the figure legends. Results from these independent experiments were reliably reproduced and multiple modes of analyses were used to cross-validate findings. For instance, results from the scRNAseq were orthogonally validated by in vivo profiling using flow cytometry or by reductionist modeling using in vitro co-culture models and bulk RNA-sequencing.
Randomization	Mice with matched sex and age were randomized into different treatment groups. No cage-specific effects were observed.
Blinding	Quantification of tumors from H&E images was done after de-identifying samples in a blinded manner. All experimental analyses were done objectively and did not require blinding.

Reporting for specific materials, systems and methods

We require information from authors about some types of materials, experimental systems and methods used in many studies. Here, indicate whether each material, system or method listed is relevant to your study. If you are not sure if a list item applies to your research, read the appropriate section before selecting a response.

Materials & experimental systems

n/a	Involved in the study
☐	☒ Antibodies
☐	☒ Eukaryotic cell lines
☒	☐ Palaeontology and archaeology
☐	☒ Animals and other organisms
☒	☐ Clinical data
☒	☐ Dual use research of concern

Methods

n/a	Involved in the study
☒	☐ ChIP-seq
☐	☒ Flow cytometry
☒	☐ MRI-based neuroimaging

Antibodies

Antibodies used

The following antibodies were used for in vivo studies:
anti-CD8a (clone 2.43, BioXCell) and the corresponding commercially-available isotype control
anti-NK1.1 (clone PK136, BioXCell) and the corresponding commercially-available isotype control
anti-IL-18 (clone YIGIF74-1G7, BioXCell) and the corresponding commercially-available isotype control
(initial dose of 200 micrograms and 100 microgram at subsequent treatments)
anti-IL-15 (clone AIO.3, BioXCell) and corresponding commercially-available isotype control
(initial dose of 200 micrograms and 100 microgram at subsequent treatments)
anti-TREM2 antibody (provided by MC) and the corresponding isotype control
(initial dose of 200 micrograms and 100 microgram at subsequent treatments)
anti-MIC-A stabilizing antibody (provided by LFA) and the corresponding isotype control (200 micrograms)
(Dilutions and dosing regimens are specified under sub-section Antibody-mediated blockade and Depletion Studies in the Methods Section.)

The following antibodies were used for flow cytometry:
CD45 (clone 30-F11, BioLegend; Cat# 103137); CD45.1 (clone A20, BioLegend); CD45.2 (clone 104, BioLegend); B220 (clone RA3-6B, BioLegend); CD19 (clone eBio1D3, eBiosciences); Ly6G (clone 1A8, BioLegend; Cat# 127621); CD64 (clone X54-5/7.1, BioLegend); MerTK (clone 2B10C42, BioLegend); CD2 (clone RM2-5, BioLegend; Cat# 100113); Siglec-F (clone E50-2440, BD Pharmingen; Cat# 740956); MHC-I-A/I-E (clone M5/114.15.2, eBiosciences; Cat# 12-5321-82); CD11b (clone M1/70, eBiosciences; Cat# 45-0112-82); CD11c (clone N418, Invitrogen; Cat# 47-0114-82); CD24 (clone M1/69; Invitrogen; Cat# 25-0242-82); CD103 (clone 2E7, BioLegend; Cat# 17-1031-82); XCR1 (clone ZET, BioLegend); CD107a (clone 1D4B, BioLegend); CD3 (clone 145-2C11, eBiosciences); CD8a (clone 53-6.7, BioLegend; Cat# 558106); CD4 (clone GK1.5, eBiosciences; Cat# 17-0041-82); CD44 (clone IM7, BioLegend); PD-1 (clone RMP1-30, BioLegend); TCF-1 (clone 7F11A10, BioLegend), Granzyme-B (clone GB11, ThermoFischer); NK1.1 (clone PK136, BioLegend); NKp46 (clone 29A1.4, BioLegend); CD49b (clone DX5, ThermoFischer); CD49a (clone HMa1, BioLegend); KLRG1 (clone MAFA, BioLegend); NKG2D (clone C7, BioLegend); TNF (clone MP6-XT22, eBiosciences; Cat# 17-7321-82); IFN-γ (clone XMG1.2, eBiosciences; Cat# 25-7311-41)
(This information is also available under sub-section Flow Cytometry and Fluorescence-Activated Cell Sorting in the Methods Section.)

The following antibodies were used for immunohistochemical staining of human tissue sections:
anti-human CD68 (clone KP1, Dako); anti-human TREM2 (clone D8I4C, Cell Signaling Technology); anti-mouse NKp46 (AF2225, BioLegend)

The following antibodies were used for immunofluorescence imaging of murine tissue sections:
anti-TREM2 (clone AF1729, R&D Systems; 1:100); anti-GFP (clone ab13970, Abcam; 1:200)
The secondary antibody used was AlexaFluor 555 donkey-anti-sheep (clone ab150178, Abcam)

Validation	All antibodies were validated for the use of immunofluorescence, immunohistochemistry, and flow cytometry. Data are available on the manufacturers' websites. For experiments shown in this study, single-stain controls and an unstained control were used to assess staining of experimental samples.

Eukaryotic cell lines

Policy information about cell lines and Sex and Gender in Research

Cell line source(s)	KP cells were obtained from Tyler Jacks and B16-OVA-MICA cells were provided by LFA.
Authentication	Cells had been sequenced by Tyler Jacks and LFA. Cells grown in-house were functionally authenticated: KP cells were intravenously injected into mice and lung tumor progression was evaluated. Prior to inoculation, cells growth in-house were assessed morphologically. No other authentication was performed.
Mycoplasma contamination	All cell lines were regularly tested for mycoplasma and confirmed to be negative for contamination prior to use.
Commonly misidentified lines (See ICLAC register)	No commonly misidentified cell lines were used in this study.

Animals and other research organisms

Policy information about studies involving animals; ARRIVE guidelines recommended for reporting animal research, and Sex and Gender in Research

Laboratory animals	The following murine strains were purchased from Jackson Laboratories and bred in our facility prior to use in this study: C57BL//6 wild-type mice C57BL/6-Trem2emAdiuj (Trem2-/-) mice B6.SJL-PtprcaPepcb/BoyJ (CD45.1) mice B6.129P2-Il18r1tm1Aki/J (Il18r1-/-) mice Mice were maintained at specified pathogen-free (SPF) health status in individually ventilated cages at 21-22 degrees Celsius and 39-50% humidity. All animal procedures were approved by the Institutional Animal Care and Use Committee (IACUC) of the Icahn School of Medicine at Mount Sinai. All mice included in this study were analyzed between 6 to 8 weeks of age.
Wild animals	No wild animals were used in this study.
Reporting on sex	Males and females were used in different experiments, with sex having been controlled.
Field-collected samples	No field-collected samples were used for this study.
Ethics oversight	Ethical and technical approval for use of mice was obtained from the Institutional Animal Care and Use Committee (IACUC) of the Icahn School of Medicine at Mount Sinai.

Note that full information on the approval of the study protocol must also be provided in the manuscript.

Flow Cytometry

Plots

Confirm that:

☒ The axis labels state the marker and fluorochrome used (e.g. CD4-FITC).

☒ The axis scales are clearly visible. Include numbers along axes only for bottom left plot of group (a 'group' is an analysis of identical markers).

☒ All plots are contour plots with outliers or pseudocolor plots.

☒ A numerical value for number of cells or percentage (with statistics) is provided.

Methodology

Sample preparation	Murine lungs were digested (see Methods Section) via mechanical and enzymatic digestion (see Methods Section), and single-cell suspensions were subjected to red blood cell lysis and filtered before staining for flow cytometry.
Instrument	BD LSRFortessa
Software	FACSDiva software v.7 (BD)
Cell population abundance	Purity of sorted populations was evaluated by flow cytometry.

Gating strategy	Macrophages from tumor-bearing lungs were gated based on a positive signal for CD64 and MerTK from a broader gate on CD45-positive immune cells that did not exhibit a positive signal for CD3, NKp46, Ly6G, CD19, and B220. Among macrophages, cells were gated based on staining for CD2 and MHC-II.

☒ Tick this box to confirm that a figure exemplifying the gating strategy is provided in the Supplementary Information.